

Effect of near-inertial pumping on subduction at an ocean front

Nihar Paul^a and Amala Mahadevan^a

^a*Woods Hole Oceanographic Institution, Massachusetts, US*

The interactions between near-inertial waves (NIWs) and submesoscale currents in the surface ocean are challenging to deconvolve due to their overlapping temporal and spatial scales. The frequency of NIW is modulated by the relative vorticity, ζ , of submesoscale currents, which varies between positive and negative ζ of $O(f)$ on spatial scales of $1 - 10 \text{ km}$, particularly across fronts where the horizontal buoyancy gradient, $\nabla_H b$, is intensified. The effective NIW frequency $f_{eff} = f + \zeta/2$ can therefore also vary by $O(f)$ on these scales, causing the waves to be out of phase. This generates periodic convergence and divergence in the surface layer, particularly at fronts. The resulting vertical motion, known as inertial pumping, is traditionally considered to be reversible. However, the strong vertical shear of the horizontal velocity at fronts, $v_z \sim |\nabla_H b|/f$, implies that not all of the water that is pumped downward will return. We examine the effect of this asymmetry on the vertical transport of tracers with an ambient vertical gradient, analogous to biogeochemical tracers, such as oxygen and dissolved organic carbon. Using numerical simulations of an unstable front forced by NIW, we demonstrate that inertial pumping can lead to net vertical transport of tracers. Spectral analysis of the vertical tracer flux – given by the covariance between tracer anomaly and vertical velocity – reveals that the interaction of strong NIW with submesoscale currents enhances the vertical exchange at the front on both the sub-inertial and inertial time scales.

Plain Language Summary

Near-inertial waves (NIWs) are ubiquitous, can propagate long distances across the ocean basin, and are known to affect turbulent mixing and dissipation within the mixed and topographic boundary layers. Past studies have shown the effect of NIWs on energy transfer across scales between balanced and unbalanced flow across a front. None of them highlights the transport of tracers in such a scenario, which can influence nutrient cycling, primary productivity, and carbon sequestration in the upper ocean. In this work, we highlight and characterize the subduction across a front driven by NIWs using process study modeling and observations collected during a Coherent Lagrangian Pathways from the Surface Ocean to Interior (CALYPSO) survey in the Balearic Sea during February-March 2022. Given the increase in storm events in ocean basins due to climate change, this study examines the potential role of NIWs in enhancing vertical transport by interacting with the submesoscale flow at scales of $0.1\text{-}10 \text{ km}$. This mechanism of enhanced transport is underestimated in coarse-resolution ocean models that are forced by smoothed wind fields.

I. INTRODUCTION

The vertical transport of momentum, heat, salt, and biogeochemical tracers plays a central role in the exchange of energy between the atmosphere and ocean, in supporting the primary production of phytoplankton, and in ventilating the stratified interior ocean [1, 33–35, 44, 48, 49, 81]. Submesoscale fronts, characterized by strong horizontal density gradients in the mixed layer and relative vorticity ζ of $O(f)$, where f is the Coriolis parameter, exert a strong influence on the vertical distribution of nutrients [19], phytoplankton, carbon, and oxygen. Frontogenesis [24] leads to the intensification of lateral buoyancy gradients and vorticity, which can give rise to vertical velocities of $O(100 \text{ m day}^{-1})$ and upwelling and subduction of surface waters at oceanic fronts [52, 58, 63, 75]. More recently, field observations and simulations suggest that turbulence in the boundary layer, coupled with frontal circulation, can further enhance subduction from the mixed layer [50].

Internal gravity waves (IGWs) also contribute significantly to the kinetic energy of the ocean. Partitioning the near-surface motions into balanced and wave components in high-resolution simulations within the MIT general circulation model [70–72] shows that in certain regions and seasons, the energy levels associated with waves are comparable to or exceed those of geostrophically balanced motions at horizontal scales of 10 to 100 km [65, 79]. IGWs — with frequencies between f and N (the buoyancy frequency) — are dominated energetically by near-inertial waves (NIWs) as seen in the kinetic energy spectrum. NIWs are often excited by winds, typically during storms or hurricanes, when winds impart momentum to the upper ocean [11–13, 30, 51]. They play a key role in the transfer of energy from the ocean surface to deeper layers, thus contributing to the global energy budget and influencing large-scale circulation and mixing [18, 78].

IGWs can also cause vertical motion of $O(100 \text{ m day}^{-1})$, but in the linear regime, the vertical excursions experienced by water parcels are reversible and do not lead to vertical transport when integrated over time. However, net transport can occur for

properties that are modified over time scales comparable to the wave period. For instance, a fraction of the nutrients uplifted into the euphotic zone by IGWs may be consumed by phytoplankton on timescales $O(1)$ day, before the nutrient-rich isopycnals subside back to depth. Turbulent mixing also leads to irreversible transport through a variety of mechanisms, including wave breaking [53] and shear-instabilities, which are modulated by ocean stratification [43, 54, 55]. Nonlinear processes become especially important when wave amplitudes are large, leading to enhanced mixing through wave–wave interactions and breaking [56].

Since submesoscale currents are characterized by their large $\zeta = O(f)$, there is a significant overlap between the motions associated with NIWs and submesoscale currents. A separation of NIWs and submesoscale currents can be done based on balanced vs. unbalanced motion [71], as well as filtering based on frequency in the Lagrangian frame [26], but the nonlinear feedbacks between waves and flow and spontaneous generation of NIWs [45] make the separation challenging [73].

One approach to examining the interaction of NIWs and submesoscale currents is through the modification of wave frequency. The frequency of NIWs ($\approx f$) is modulated by the ζ of the background flow, to result in an effective frequency $f_{\text{eff}} = f + \zeta/2$ [31, 77, 80]. At submesoscales, the effective frequency of NIW can differ significantly (by $O(f)$) on either side of a front, since the denser side typically has positive (cyclonic) ζ and the less dense side of the front has negative (anticyclonic) ζ , both of which can be $O(f)$, although typically, the cyclonic vorticity is larger than the anticyclonic vorticity at submesoscale fronts. Consequently, the NIWs have different frequencies on either side of the front, resulting in a phase difference between cyclonic and anticyclonic regions that changes with time. This leads to periodic horizontal convergence and divergence when the waves are out of phase, resulting in periodic vertical motion, sometimes referred to as inertial pumping, which is often focused at fronts.

Inertial pumping occurs when NIWs interact with a flow that has spatially varying vorticity and serves to transfer energy downward from the NIW field in the mixed layer to IGW in the stratified pycnocline. Its effect on the vertical transport of tracers has not received much attention in the literature, and previous studies based on high-resolution model simulations with wind-generated NIWs do not show evidence for such transport [2]. However, strong lateral buoyancy gradients, $|\nabla_H b|$, where b is the buoyancy, associated with submesoscale flows are in approximate thermal wind balance and generate strong vertical shear in the horizontal velocity $|\mathbf{u}_z| \approx f^{-1} |\nabla_H b|$. This would imply that a tracer that is moved vertically downward from the surface due to inertial pumping would experience a different horizontal transport than at the surface, and the vertical transport may not necessarily be reversible in the opposite phase of the wave divergence. In a spatially variable submesoscale flow that evolves on inertial time scales, such a rectification effect can lead to net vertical transport of tracers with a strong vertical gradient.

The aim of this study is to examine whether the interaction between wind-generated near-inertial waves and submesoscale frontal flows leads to a net downward tracer transport that exceeds the frontal transport in the absence of the waves. Recent field observations of a submesoscale frontal jet in the Alboran Sea in the Western Mediterranean under highly variable wind conditions found that drifters exhibit time-dependent divergence associated with NIWs [17]. This study extends the simple model used in [17] to a fully three-dimensional submesoscale-resolving frontal flow with strong NIWs to test the hypothesis that NIWs can enhance the vertical transport at fronts. A semi-idealized front, representative of conditions in the western Mediterranean, is forced, initially, by inertial winds to generate NIWs that are allowed to evolve freely within the baroclinically unstable flow field.

The model is used to examine the vertical transport of a passive tracer that is initialized to vary linearly with depth. NIWs in the surface mixed layer lead to increased shear at the base of the mixed layer, which would generate diapycnal vertical transport through mixing. Since this study focuses on transport along isopycnals, the model’s vertical eddy diffusivity, κ_v , is set to a uniform and constant value of $\kappa_v = 10^{-5} \text{ m}^2 \text{ s}^{-1}$ throughout the model domain. To minimize the influence of nonlinear Ekman pumping [8, 46, 64, 69], the tracer field is initialized only after the wind forcing is turned off, and our analyses are for the period when the front as well as NIWs are unforced and decaying.

The manuscript is organized as follows: we describe the model configuration and numerical experiments in Section II. Section III presents model results, where the near-surface flow and associated subduction are characterized through estimates of tracer deficit in Sections III A, III B, followed by probability density functions (PDFs) of vorticity, divergence, and horizontal buoyancy gradient in Section III C. Next, we examine the isotropic wavenumber power spectral density (PSD) of horizontal and vertical kinetic energy, along with the ratio of vorticity PSD to divergence PSD (Section III D). The frequency–wavenumber dispersion characteristics of vertical velocity are analyzed in Section III E. In Section III F, we describe the mechanism of NIW-driven subduction, and Section III G focuses on vertical tracer covariance spectra. Finally, Section IV summarizes the results.

II. MODEL CONFIGURATION AND INITIALIZATION

We use the non-hydrostatic Process Study Ocean Model (PSOM) [36, 37] to simulate a front in a zonally periodic channel. The north-south vertical section of the model is initialized with the temperature-salinity structure of a salinity-controlled mesoscale front (measured to 250 m depth during March 2022) in the Balearic Sea in the western Mediterranean Sea, shown in Fig. S1a [10]. An Argo profile is used to initialize the model from a depth of 250 m to 1000 m . The corresponding potential temperature (θ , $^{\circ}C$), salinity (S , psu), and squared buoyancy frequency (N^2 , s^{-2}) with the contours of the potential density are shown in Fig. S1b-d. A PDF of the horizontal buoyancy gradient $M^2 = |\nabla_H b|$ — where $b = -g(\frac{\rho - \rho_0}{\rho_0})$ is the buoyancy, ρ is the potential density, $g = 9.81 \text{ m s}^{-2}$ is the acceleration due to gravity, and $\rho_0 = 1027 \text{ kg m}^{-3}$ is a reference density — is shown in Fig. S1e. The front is initialized with a mixed layer depth (MLD) of 25 m (35 m) on the lighter side (heavier), and stratification of $\mathcal{O}(10^{-5}) \text{ s}^{-2}$ typical of winter conditions of 30-60 m in the Balearic Sea [74] shown in Fig. S2a,b-e. The initial condition features a small-amplitude meander with one wavelength in the zonal direction, which triggers baroclinic instability.

The model domain is centered at $40.5^{\circ}N$, where the inertial period is 18 *hours*. The model domain extends 96 km in the (periodic) x direction, 192 km in the y -direction with closed walls and free-slip boundary conditions, and 1,000 m in depth. The horizontal resolution is 1000 m , with a stretched grid in y that achieves a spacing of 2 km within 40 km of the solid boundaries in the north and south. There are 64 vertical levels on a stretched grid with spacing ranging from 0.5 m near the surface to 54 m at the deeper depth. The model time step is 432 s .

Three types of numerical experiments are conducted (Table I). In the first case, F, the density front is allowed to evolve freely without any surface forcing. In the second and third cases, the surface is forced by an inertial wind with zonal wind stress $\tau_x = a_0 \sin(ft)$ and meridional wind stress $\tau_y = a_0 \cos(ft)$ from day 5 to day 8 for four inertial periods. The amplitude of forcing (a_0) is weaker (maximum of 0.03 Pa) in the case F + WW, and stronger (maximum of 0.05 Pa) in the case termed F + SW. The wind stress in the forcing time interval (day 5–8) is multiplied by a Tukey window with a cosine fraction of 0.1 to smoothly transition the forcing between 0 and the maximum value. Furthermore, the meridional (y -direction) profile of wind stress is tapered using a tanh profile within 48 km of the northern and southern boundaries to prevent any concentrated up-/down-welling in the grid cell closest to the wall boundaries. The experiments are run for a total of 60 *days*, and the corresponding forcing profile is shown in SI Fig. S3.

Model run	F	F + WW	F + SW
Max wind forcing	None	0.03 Pa	0.05 Pa
KE_w/KE_m	-	40	120

TABLE I: Three sets of numerical experiments are conducted. Case F is just the front without any forcing. In the other two experiments, the front is initially forced by winds. Case F + WW has weaker waves, and case F + SW has stronger waves. The wind is applied as an inertial stress over 4 inertial periods and is ramped up and down with a Tukey window. KE_w/KE_m is the ratio of the wave to mean components of the kinetic energy right after the wind forcing is applied.

The horizontal diffusion of momentum and tracers is $1 \text{ m}^2 \text{ s}^{-1}$. After the winds are turned off (from day 8 onward), the vertical diffusivity, $\kappa_v = 10^{-5} \text{ m}^2 \text{ s}^{-1}$ throughout the domain. During the time of wind forcing (day 5–8) $\kappa_v(z)$ is a prescribed as a function of windstress [23, 38] according to $\kappa_v = \max[\kappa_{max}[1 + \tanh(\frac{z+\delta_e}{\Delta})], \kappa_{min}]$, where $\delta_e = \frac{0.4}{f} \sqrt{\frac{\tau}{\rho_0}}$, is the surface Ekman depth and $\Delta = 0.5\delta_e$. The windstress magnitude is τ , $\kappa_{min} = 10^{-3} \text{ m}^2 \text{ s}^{-1}$ and $\kappa_{max} = 10^{-5} \text{ m}^2 \text{ s}^{-1}$. The model has a flat bottom and a linear bottom drag of 10^{-5} m s^{-1} . The density is adjusted to a stable state by convective adjustment.

A tracer with concentration $c \text{ (mg m}^{-3}\text{)}$ is initialized as a linear profile ranging from 1 at the surface to 0 at the bottom (SI Fig. S2h) after the winds are turned off on day 8. The model analysis is performed from days 8 to 60 of the model simulation.

The density front is initialized with a high local Rossby number, $Ro = \zeta/f$, defined as the ratio of vertical relative vorticity, $\zeta = v_x - u_y$, to f , is initially $\mathcal{O}(2)$. The frontal lateral buoyancy gradient $M^2 = |\nabla_H b|$ normalized by f^2 has an initial value of $M^2/f^2 = 101.13$, where $f = 9.45 \times 10^{-5} \text{ s}^{-2}$. This results in an initial surface rms velocity $u_{rms} = 10 \text{ cm s}^{-1}$ (SI Text 1). The initial Richardson number $= N^2/U_z^2 = 0.3$ at the base of the MLD $H = 25 \text{ m}$ and $N^2 = 2 \times 10^{-4} \text{ s}^{-2}$ on the lighter side of the front. The maximum ratio of wave kinetic energy to mean kinetic energy $\Gamma = KE_w(\omega > 0.8f)/KE_m(\omega < 0.8f)$ is 40 and 120 for $|\tau| = 0.03$ and 0.05 Pa , respectively, for the front with weak waves (F+WW) and the front with strong waves (F+SW). In the following section, we compare the dynamics of the front-only case, F, with the F+WW and F+SW cases.

One way to examine the flow is in terms of the rotational and irrotational (divergent) parts of the velocity field. The Helmholtz decomposition is used to partition the horizontal velocity (u, v) into rotational u_r, v_r and divergent u_d, v_d components as

$$u = u_r + u_d = -\psi_y + \phi_x, \quad v = v_r + v_d = \psi_x + \phi_y, \quad (1)$$

where the stream function ψ and the velocity potential ϕ are such that

$$\nabla_h^2 \psi = \zeta = v_x - u_y \quad \text{and} \quad \nabla_h^2 \phi = \delta = u_x + v_y. \quad (2)$$

In what follows, we apply this decomposition to the kinetic energy.

III. RESULTS

A. Near-surface evolution of velocity

In time, the front becomes unstable, exhibiting meanders and generating eddies with diameters of approximately 20–30 *km*, along with filamentary structures (Fig. 1a-c). In the F+WW and F+SW experiments, inertial wind forcing applied between days 5–8 excites oscillations that develop into NIWs (Fig. 1d-f). While the phase propagates upward, wave energy propagates downward, energetically dominating the flow throughout the 60-day simulation. The wave amplitude gradually decreases over time. The vorticity of the frontal flow strongly modulates the NIWs, which, in turn, exert a significant influence on both the rotational (vorticity-dominated) and divergent components of the circulation.

The vertical component of the relative vorticity, ζ , reaches values of $O(f)$ at the front, consistent with submesoscale dynamics. After the waves attenuate, the weak-wave (F+WW) and strong-wave (F+SW) cases exhibit vorticity magnitudes comparable to those of the front-only (F) case (Fig. 1a-c), but in these cases, eddies develop faster and become larger than in the case F (Fig. 1(a-c)). At 3.5 *m* depth, the area-averaged rotational kinetic energy (KE) is elevated in the wave-forced cases compared to the F-only run immediately after inertial forcing, and accompanied by a strong divergent KE signal that gradually decays over the 60-day integration (SI Fig. S4). Notably, during the final 20 *days*, rotational and divergent KE remain nearly an order of magnitude higher in the wave-forced cases, suggesting that there is an exchange of energy between the balanced and unbalanced components of the circulation [7, 47, 66]. External forcing at low wavenumber governs the exchange of energy between the balanced and unbalanced components of the flow through a complex interplay of wave-mean flow interactions and nonlinear turbulent processes [9, 21, 39]. The resulting envelope is strongly scale-dependent, delineating the transition between slow and fast dynamics as the simulation evolves (SI Fig. S4).

The Hövmöller diagrams of vertical velocity, w with depth in the upper 100 *m* at the domain center (Fig. 1d-e) shows substantially higher w of alternating sign in the F+WW and F+SW cases, reaching $\sim 60 \text{ m day}^{-1}$, compared to only 20 *m day*⁻¹ in the F case. The waves lift and lower the isopycnal surfaces (black contours), in contrast to the w in the F case, which is primarily aligned along isopycnals [20]. In the F+WW and F+SW cases, a downward propagation of wave energy is evident, with a downward component of group velocity of approximately 3–5 *m day*⁻¹. The Hövmöller diagrams of horizontal and vertical KE in SI Fig. S5 and S6 indicate that wave forcing enhances energy in the upper 100 *m*. Additionally, waves reflect off the bottom boundary and meridional walls, propagating upward, as shown in Fig. 1f. Overall, the simulations demonstrate the propagation pathways of NIWs generated by wind forcing, capturing both downward and upward energy fluxes. Such behavior is qualitatively consistent with subsurface moored observations of wind-induced internal waves interacting with mesoscale frontal features, for example, in the central Sea of Japan [27].

B. Tracer transport

Most biogeochemical properties have a vertical gradient in the upper ocean. We therefore use an idealized passive tracer, $c(x, y, z, t)$, initialized on day 8 when the wind stress is turned off, with a linear, horizontally uniform, profile $c_i(z)$, ranging from 1 at the surface to 0 at the seabed. The normalized tracer deficit, $D = (c(x, y, z, t) - c_i(z))/c_i(z)$ is indicative of

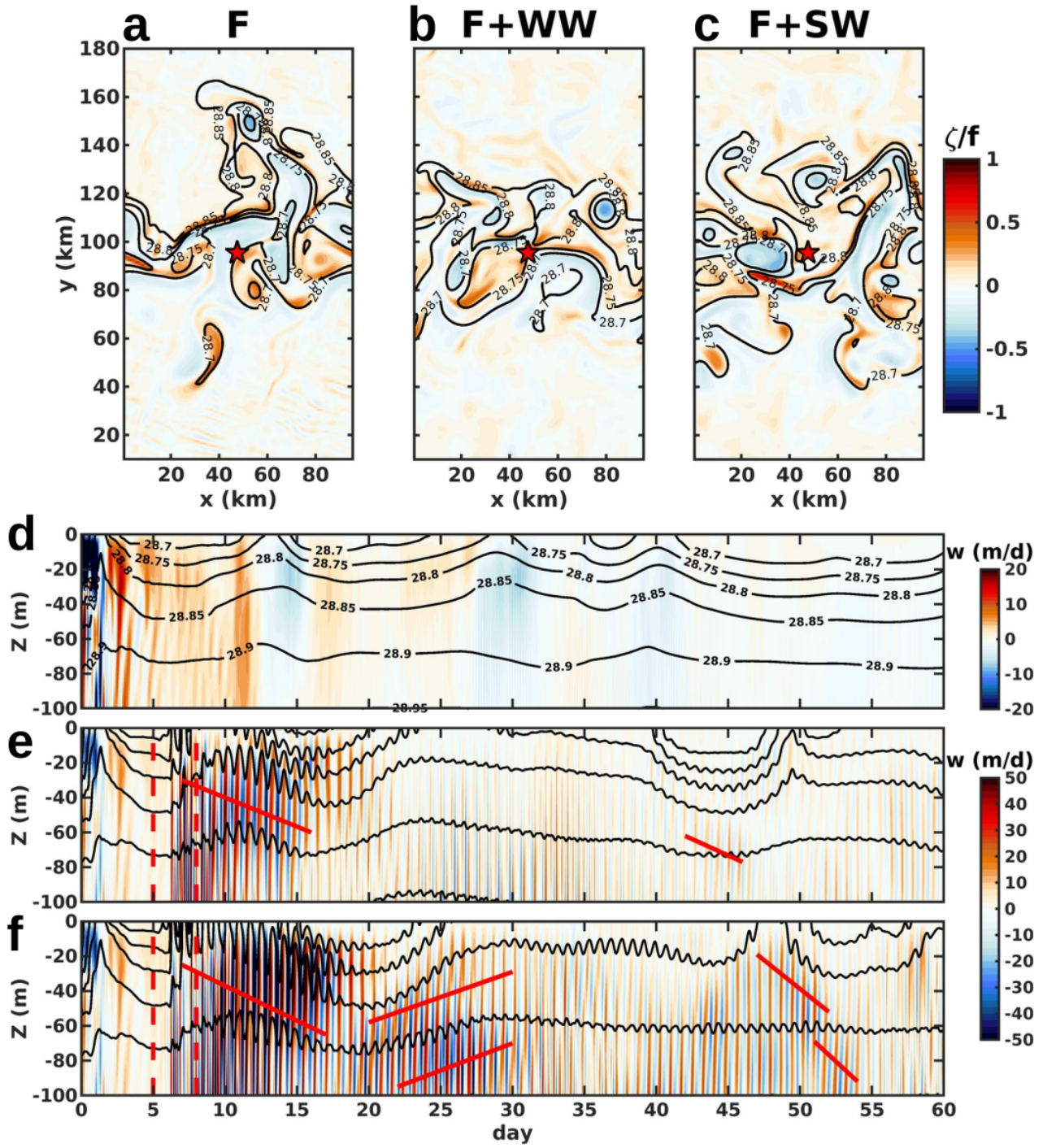


FIG. 1: Panels (a–c) show the relative vorticity, ζ , normalized by f , overlaid with potential density contours at a depth of 3.5 m on Day 60 for the three cases: the front (F), front with weak waves (F+WW), and front with strong waves (F+SW). By Day 60, the wave energy has greatly attenuated. Panels (d–f) are time series of the vertical velocity (w) in the upper 100 m with potential density contours (black) at the domain center marked by a star, for the same cases: (d) F, (e) F+WW, and (f) F+SW. In panels (e) and (f), the vertical dashed lines indicate days 5–8, during which time the inertial wind stress is applied. The solid red lines in panels (e) and (f) correspond to a group velocity on the order of 3–5 $m day^{-1}$.

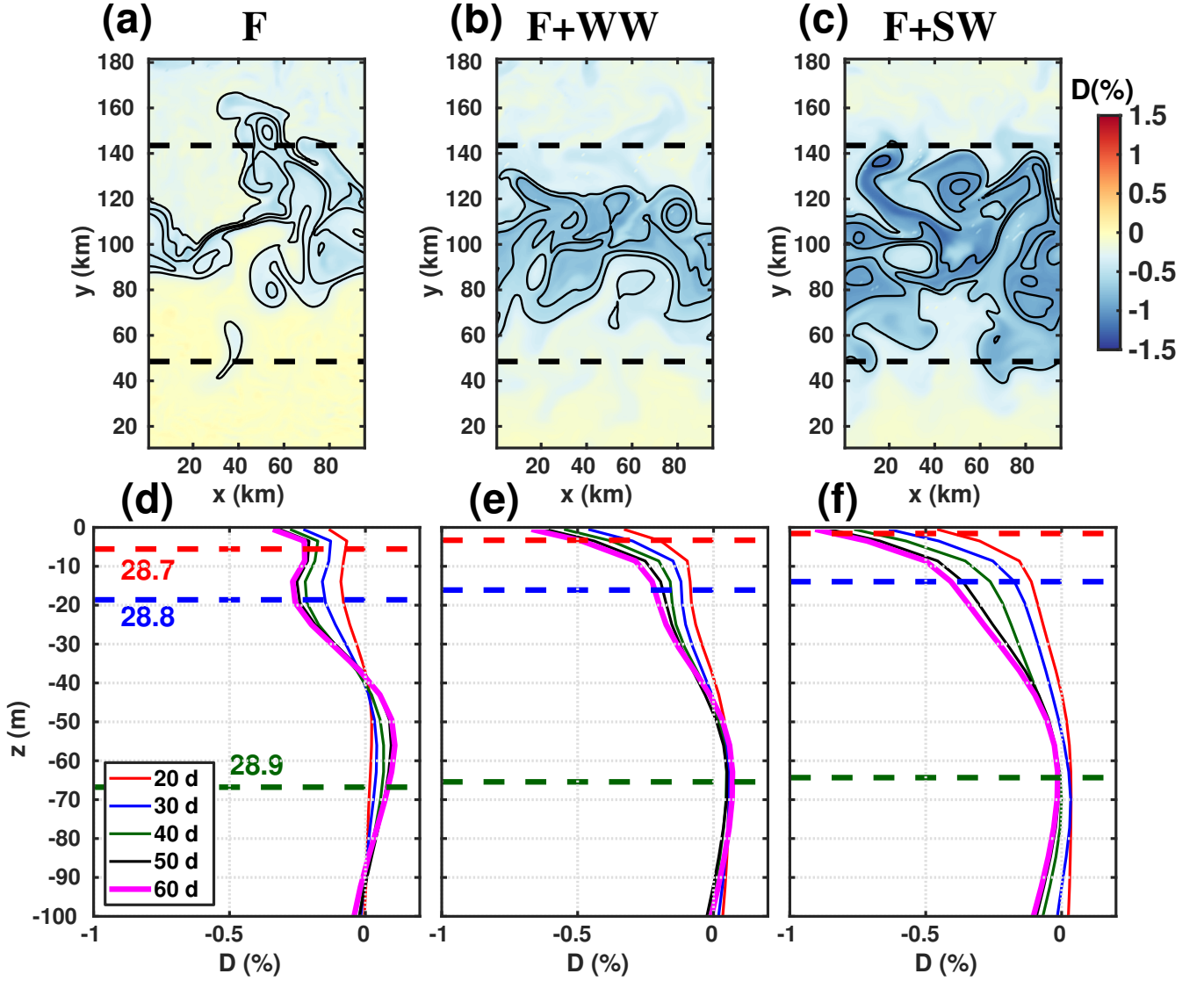


FIG. 2: Panels (a–c) show the spatial distribution of tracer deficit (D , in %) on Day 60 relative to Day 8 when the tracer is initialized, for the three cases: Front (F), front with weak waves (F+WW), and front with strong waves (F+SW). Potential density anomaly contours at 3.5 m are overlaid in each panel for day 60. The horizontal dashed lines indicate $y = 48$ km and 144 km, which mark the meridional extent of the region used for horizontal averaging. Panels (d–f) horizontally averaged vertical profiles of the tracer deficit, $D\%$, over the upper 100 m. The averaged isopycnal depths for 28.7 (red), 28.8 (blue), and 28.9 kg m^{-3} (green), computed relative to 3.5 m depth on Day 60, are also shown for all three cases.

cumulative vertical transport (Fig. 2). A comparison of the horizontal distribution of $D(x, y, z, t)$ near the surface ($z = -3.5$ m) between the three model runs F only, F+WW, and F+SW in (Fig. 2a–c), shows that NIWs enhance the vertical transport at the front and the vertical transport of tracer is largest for the case F+SW. Away from the frontal zone in which horizontal buoyancy gradients are present, the waves make little or no impact on vertical transport.

The tracer deficit (D), averaged zonally and meridionally between $y = 48$ and 144 km (Fig. 2d–f), indicates that tracer anomalies in the upper 100 m increase over time as the tracer is transported down-gradient from the surface to the interior. Because the tracer is conserved in these model runs, its depletion from the upper ocean is compensated by accumulation at depth. The upward transport of a tracer whose concentration increases with depth can be expressed as $1 - c$. A comparison across model runs reveals that when NIWs interact with the front, as in the F+WW and F+SW cases, the vertical tracer transport from the upper 10 – 25 m is enhanced by a factor of 3 – 4 relative to case F. The isopycnal depths associated with 28.7 , 28.8 , and 28.9 kg m^{-3} shoals on day 60 m in the wave-forced cases compared to the front evident from Fig. 2d–f. Because our model does not include turbulence within the mixed layer, we use isopycnal depth as a reference for assessing the depth of tracer

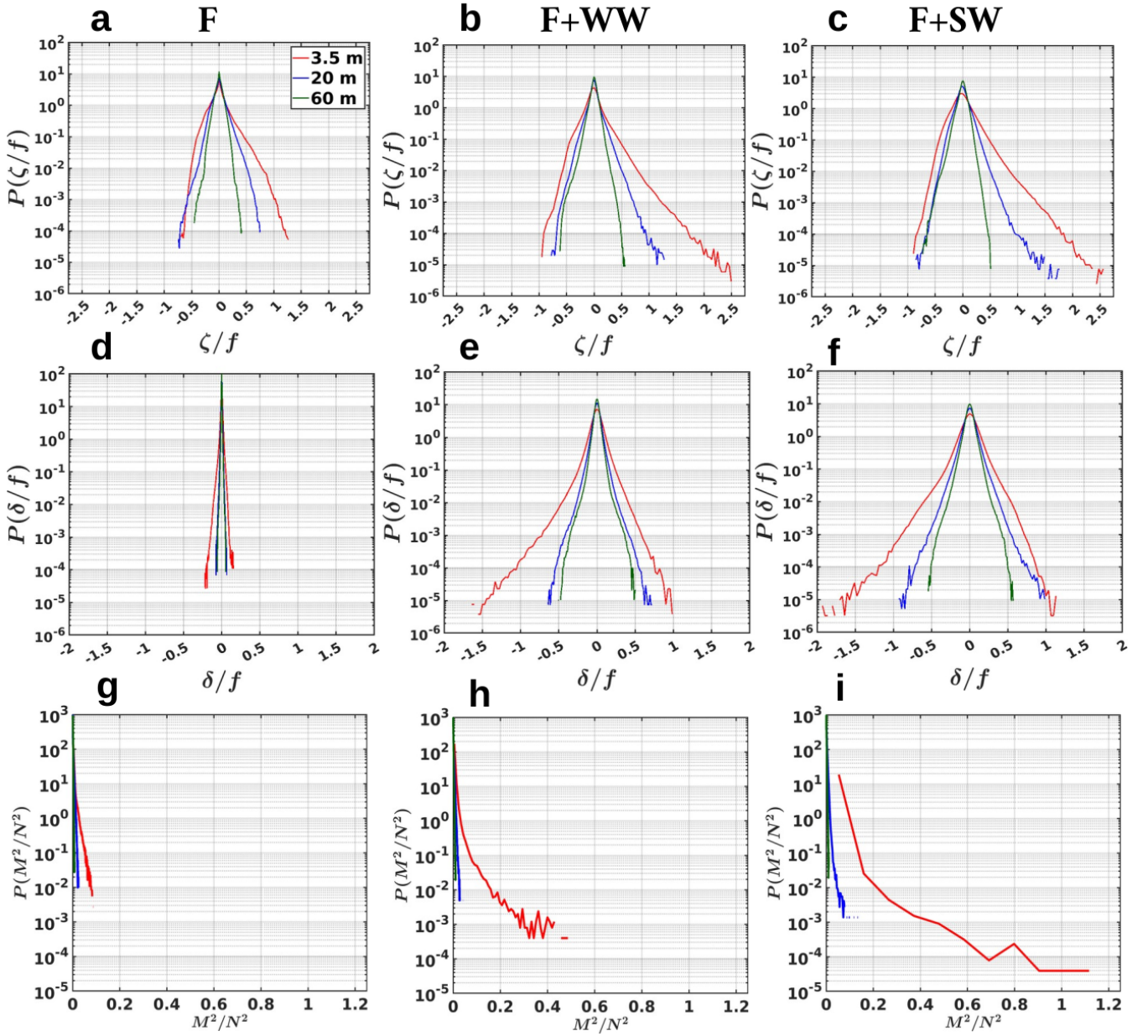


FIG. 3: Probability density functions (PDFs) of (a–c) normalized relative vorticity ζ/f ; (d–f) horizontal divergence δ/f , where $\delta = u_x + v_y$; and (g–i) ratio of magnitude of the horizontal buoyancy gradient (M^2) and vertical stratification (N^2) given by $M^2/N^2 = |\nabla_H b|/\partial b/\partial z$, b is the buoyancy. The left column is the front-only case (F), the middle column – front with weak waves (F+WW), and the right column – front with strong waves (F+SW). The PDFs are computed over the period from Day 8 to Day 60, after the winds are turned off, at depths of 3.5 m (red), 20 m (blue), and 60 m (green).

transport. In the later part of the analysis, we therefore focus on the near-surface $z=3.5$ m, 20 m, and at 60 m depth relative to the initial average MLD of 30 m set by the front. A representative set of simulations—comparing a front without NIWs, a front with NIW forcing, and a case without a front but with background stratification—shows that substantially more tracer is transported when both the front and NIWs are present than in the other cases (SI Movie S1).

C. Vorticity, divergence, and isopycnal slope

Submesoscale dynamics is known to locally intensify the lateral buoyancy gradient $M^2 = |\nabla_H b|$ through frontogenesis [4, 41], as well as the relative vorticity ζ and divergence $\delta = u_x + v_y$ in the near-surface layer [3, 62]. The PDFs of ζ , δ , and isopycnal slope M^2/N^2 (Fig. 3) for the F, F+WW, and F+SW cases highlight the characteristic intensification of these quantities near the surface (3.5 m), at 20 m, and 60 m. The PDFs are computed from days 8 to 60, after the wave-forced cases' inertial wind forcing is turned off. Within the mixed layer, the relative vorticity distribution is positively skewed, with filaments of strong cyclonic vorticity embedded in a weaker, predominantly anticyclonic background. This positive skewness decreases with depth and is largely diminished below the mixed layer. In contrast, the PDF of δ is negatively skewed, reflecting stronger convergence, with the skewness weakening with depth.

In particular, the presence of waves in the F+WW and F+SW cases substantially enhances the relative vorticity and its positive skewness (Fig. 3b,c), as well as the divergence and its negative skewness (Fig. 3e,f). The increased occurrence of large positive vorticity and negative divergence in these cases is consistent with the greater isopycnal slopes, reflected by higher values of M^2/N^2 , relative to the F-only case. This indicates that NIWs not only locally amplify vorticity and divergence at the front but may also intensify frontogenetic processes [24]. Consequently, the enhanced vertical velocities arise from a combination of wave-induced motions and strengthened secondary circulations at the fronts.

D. Power spectral density (PSD) of horizontal KE, vertical KE, and $PSD(\zeta)/PSD(\delta)$

The isotropic PSDs of horizontal kinetic energy (KE) are calculated within the domain along the zonal direction and 48 km from the north-south boundaries, that is, 96×96 km. The velocities are tapered in the y-direction using a Tukey window with a cosine fraction of 0.1, and the mean area is removed at each time step. Then, consecutive isotropic spectra are calculated following the methodology described in the SI text 2. The results show the spectra at depths of 3.5 m, 20 m, and 60 m which are calculated for each timestep and averaged from day 8-60.

The isotropic PSD for the horizontal kinetic energy (KE), the vertical KE (Fig. 4a-c and d-f, respectively), reveals differences between the frontal flow (F) and the front with NIWs (F+WW and F+SW). The energy levels are considerably higher for cases with NIWs. The PSD of the KE associated with u, v rolls off from $E_h(K) \sim K^{-2}$ to $E_h(K) \sim K^{-3}$ with increasing K (Fig. 4a-c), where, $K = \sqrt{k_x^2 + k_y^2}$ is the isotropic wavenumber with k_x and k_y the zonal and meridional wavenumber, consistent with previous studies of quasi-geostrophic turbulence and submesoscale currents [7]. The spectrum of the vertical KE $E_v = \frac{1}{2}w^2$ steepens from $E_v(K) \sim K^0$ to $E_v(K) \sim K^{-1}$ with increasing K (Fig. 4d-f). Unlike the horizontal KE, the vertical KE is higher below the surface, since even though we expect the divergence $u_x + v_y$ to be highest near the surface, $w(z) = \int_z^{surface} (u_x + v_y) dz$. The vertical KE is almost two orders of magnitude higher for the cases with NIWs, and is particularly high for the F+SW case.

All the spectra constructed from our model exhibit a roll-off and spurious fluctuations at high wave numbers. The front case shows spurious fluctuations below $K = 1/8 \text{ km}^{-1}$, which suggests that the model does not properly represent energy at horizontal scales below 8 km as it lacks a subgrid turbulence closure scheme besides a small and uniform eddy viscosity. The F+WW and F+SW cases show spurious fluctuations or roll-off for $K = 1/4 \text{ km}^{-1}$, but we chose a scale cut-off of 8 km (shaded gray in Fig. 4) for consistent comparison between model runs. Furthermore, the deformation radius (L_R) is approximately $L_R = NH_m/f = 14 \text{ km}$, where H_m is the depth of the mixed layer (the depth corresponding to the maximum N , where N is calculated as the average of all grid points within the domain of the isospectra from day 8 to day 60), and this number is in good agreement with altimetry estimates in the Balearic Sea [40].

Submesoscale velocities are comprised of vortical geostrophic and ageostrophic motions, and the contribution of IGWs [5, 6, 32]. The divergence includes contributions of both submesoscale ageostrophic motions and IGWs. The PSD of vorticity and divergence (SI Fig. S7) for the F, F+WW, and F+SW cases shows that waves slightly increase the power in vorticity and significantly increase the power in divergence.

The spectrum of half of the vertical vorticity square, also defined as the enstrophy, represents the geostrophically balanced part of the KE, and the square of the divergence yields the unbalanced dynamics. The power spectrum of relative vorticity, $RV = \zeta/f$, can be considered as the vortical contribution to the KE given by $|RV(K)|^2 = \frac{K^2|\psi(K)|^2}{f^2}$, and $K^2|\psi(K)|^2$ is the

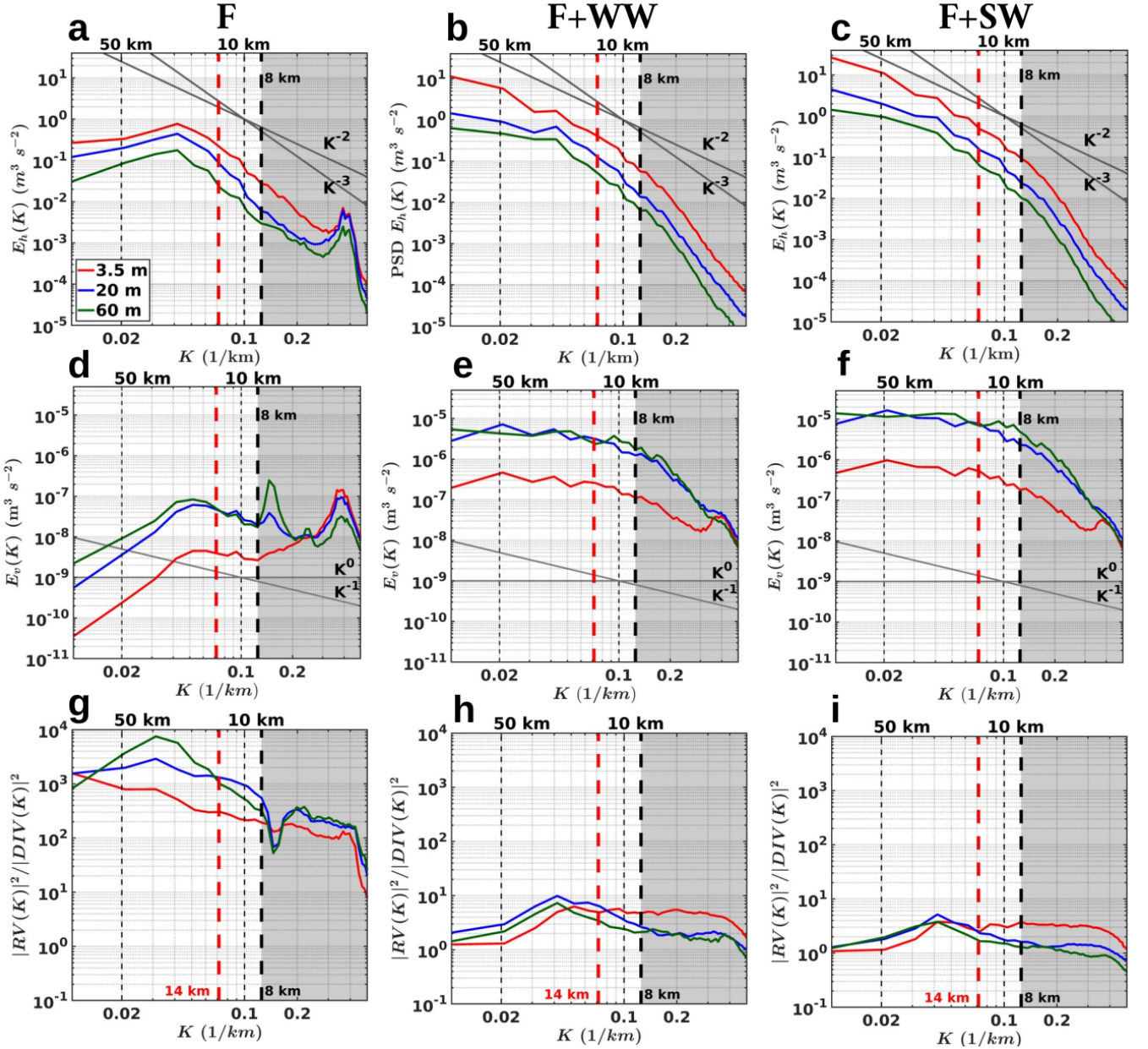


FIG. 4: Panels (a–c) show the isotropic power spectral density (PSD) of horizontal kinetic energy, (d–f) vertical kinetic energy, and (g–i) the ratio of PSD of relative vorticity (RV) to PSD of divergence (DIV), all averaged over Days 8–60. The spectra are plotted as a function of horizontal wavenumber ($K = \sqrt{k_x^2 + k_y^2}$, where k_x and k_y are the zonal and meridional wavenumbers, respectively, at depths of 3.5 m (red), 20 m (blue), and 60 m (green). Results are shown for the three cases: the front (F), the front with weak-wave forcing (F+WW), and the front with strong-wave forcing (F+SW). Reference slopes of $\{-3, -2\}$ for horizontal kinetic energy (a–c) and $\{-1, 0\}$ for vertical kinetic energy (d–f) are indicated. The grey-shaded region to the right of 8 km (thick black vertical dashed line) marks the unreliable part of the PSD based on visual inspection. The red dashed line denotes the Rossby radius of deformation (L_R).

vortical component of the KE spectrum. Using a similar argument, the power spectrum of the lateral divergence, $DIV = \delta/f$, yields $|DIV(K)|^2 = \frac{K^2 |\phi(K)|^2}{f^2}$, where $K^2 |\phi(K)|^2$ is the divergent component of the KE spectrum. Waves significantly decrease the ratio of their PSDs, i.e., $|RV(K)|^2 / |DIV(K)|^2$ (Fig. 4g–i) as they make an outsize contribution to horizontal divergence.

In the context of NIWs, energy transfer across scales can lead to a reduction in the inverse KE cascade of the low-passed eddy flow and an enhancement in its forward cascade. At larger spatial scales, the forward KE cascade of NIWs is accomplished

through wave scattering and direct extraction by rotational eddy motions. In comparison, on smaller spatial scales, it is also dominated by wave-wave interactions [61]. In the given scenario, the nonlinear interaction of NIWs and eddies can result in distinct spectral characterizations in the wavenumber-frequency space within and below the initial mixed layer, which is examined in the following section.

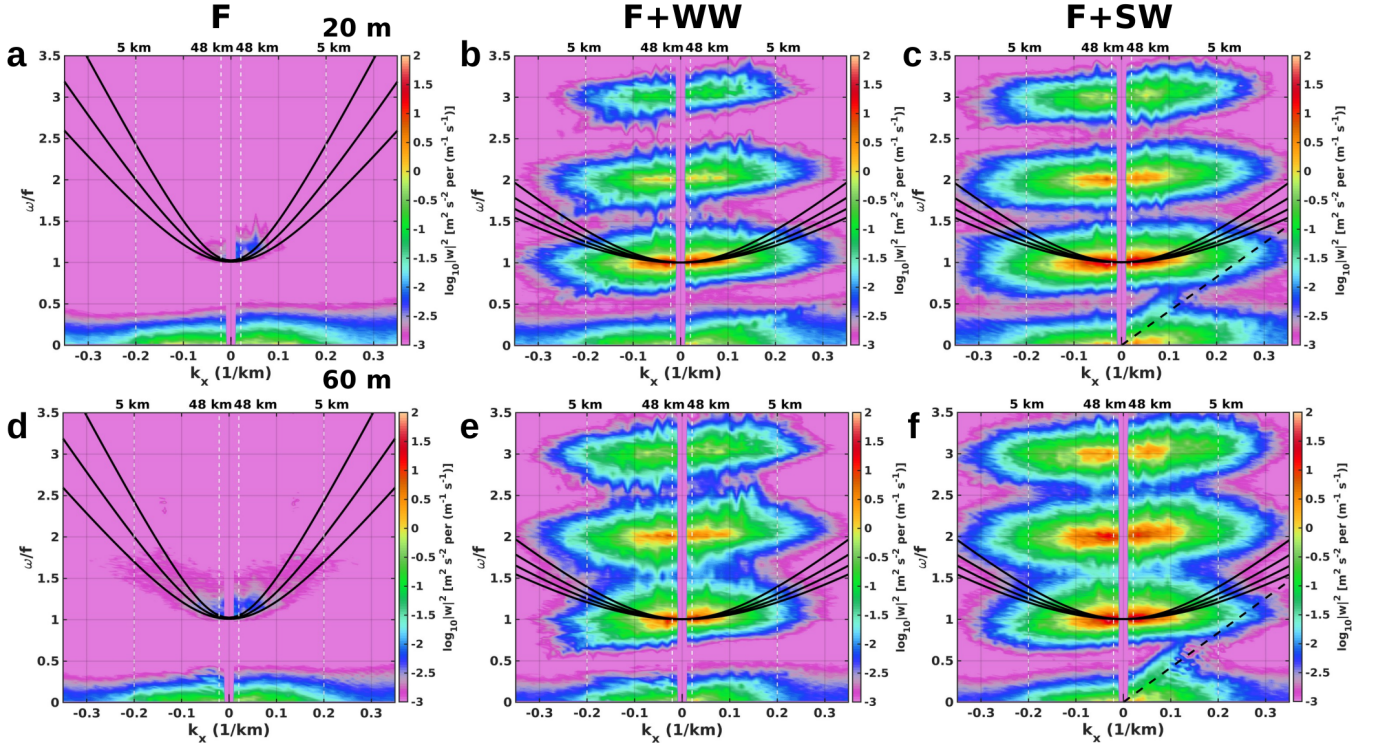


FIG. 5: Panels (a–c) and (d–f) show the zonal wavenumber (k_x)–frequency (ω/f) power spectral density of vertical velocity, meridionally averaged, for the F, F+WW, and F+SW experiments at 20 m (top row) and 60 m (bottom row), over days 8–60. Overlaid dispersion curves correspond to channel mode $n = 8$, with baroclinic phase speeds (c_m) for modes $m = 3 - 5$ in F (upper to lower curves), and modes $m = 7 - 10$ in F+WW and F+SW (upper to lower curves). In the F+SW case, the black dashed line marks the baroclinic phase speed of the Kelvin wave along the channel boundary, empirically fitted as 0.063 m s^{-1} .

E. Frequency-wavenumber iso-spectra of vertical velocity

The solid walls at the northern and southern boundaries of the domain inevitably support channel modes in the internal gravity wave field [22]. To evaluate their influence, as well as the distribution of wave energy across dispersion characteristics, we compute the vertical velocity zonal-wavenumber (k_x)-frequency (ω/f) power spectral density for the F, F+WW, and F+SW experiments (Fig. 5), evaluated at 20 m (top row) and 60 m (bottom row). First, the variables are tapered in time, and then the time-average of the variable at each point in the grid is subtracted to obtain anomalies. The power spectral density is computed using a 2D FFT along the time and zonal directions, and the result is averaged meridionally for both depths.

The dispersion relation for Poincaré internal waves in a channel of finite depth H and finite width W , subject to no-normal-flow meridional boundary conditions [22], is given by

$$\omega^2 = f^2 + c_m^2 K^2 = f^2 + c_m^2 (k_x^2 + n^2 \pi^2 / W^2) \quad (3)$$

where ω is the frequency, $W = 192 \text{ km}$ is the channel width, k_x is the zonal wavenumber, n is the meridional mode number (an integer), and c_m is the baroclinic wave speed of the vertical mode m . The term $n\pi/W$ represents the meridional wavenumber

imposed by the channel boundaries, giving rise to discrete meridional (channel) modes, while k_x remains continuous in the zonal direction. Each vertical mode m has its own baroclinic wave speed c_m , which governs the horizontal propagation of the waves. The dispersion curves for $m = 3, 4, 5$ overplotted in Fig. 5 suggest that these channel modes are present in the model simulations.

Stratification profiles, $N^2(z)$, are computed from time-averaged densities at each grid point between days 8 and 60 across the domain. These profiles are then used as input to the Sturm–Liouville problem [28, 29, 42] derived from the linearized Boussinesq equations with f at 40.5°N and a water depth of 1000 m . The corresponding $\overline{N^2(z)}$, along with the barotropic ($m = 0$) and the first ten baroclinic wave speeds ($m = 1 - 10$), are shown in SI Fig. S8, while the associated vertical eigenfunctions are presented in Fig. S9 for the three experiments. Stratification is weaker in the F+WW and F+SW cases compared to F alone. Consequently, the baroclinic wave speeds are slightly reduced relative to F. Increasing the vertical grid resolution, however, may produce more substantial differences in the estimated baroclinic speeds (see SI Table 1).

Even though experiment F is unforced, frontal adjustment leads to some spontaneous generation of NIWs, with the energy spectral density showing distinct subinertial and inertial energy packets. We focus on channel mode $n = 8$, corresponding to a meridional length scale $l_y = 2W/n = 48\text{ km}$ [22]. As shown in Fig. 5a,d for depths of 20 m and 60 m , the energy packets in the F experiment are concentrated within vertical modes $m = 3 - 5$. In contrast, in the wave-forced cases (F+WW and F+SW; Fig. 5b,e, and Fig. 5c,f), the energy packets are more dispersed along the zonal wavenumber axis and are shifted toward higher vertical modes ($m = 7 - 10$). Additionally, both wave cases show changes in power at subinertial frequencies and the scattering of energy into superinertial harmonics ($2f, 3f, \dots$). We also empirically fit a line corresponding to the baroclinic wave speed of 0.063 m s^{-1} , which represents the effect of the boundary-trapped Kelvin wave that decays offshore within a Rossby radius of deformation. Overall, the scattering of NIW energy toward higher frequencies is consistent with idealized quasi-geostrophic (QG) simulations by [14] and global-scale numerical simulations by [57], indicating nonlinear wave–wave interactions that facilitate energy transfer across scales. The following section examines how the enhanced vertical velocities induced by these waves interact with submesoscale currents to generate convergence and divergence.

F. Mechanism of subduction by NIWs

In this section, we examine the influence of waves on the evolution of ocean fronts. Averaged over the model domain, the temporal evolution of M^2 at the surface (Fig. 6a) over the 60-day period of the simulation shows that the mean M^2 is enhanced in the strong wave cases relative to the weak wave instances, suggesting that NIWs can modify the lateral buoyancy gradients during front evolution. Interestingly, the average M^2 evolved in both wave cases is bounded within, compared to the F case. Although for the SW case, M^2 shoots above the F case around day 35, indicating that the dynamics associated with frontogenesis may start to play a role in this case. However, the most pronounced wave effects appear through divergence and convergence, driven by the enhanced divergent component of the flow in the case of the waves.

Frontogenetic strain also contributes to the intensification of lateral buoyancy gradients, with the rate quantified by the advective frontogenetic tendency, $F_{adv} = \mathbf{Q} \cdot \nabla_H b$. In the context of adiabatic, hydrostatic, and Boussinesq flow (as described by Equation 4), \mathbf{Q} represents the strain vector of the horizontal velocity field. This frontogenetic forcing mechanism drives the ageostrophic secondary circulation that is characteristic of front development [24, 25, 67]. This diagnostic distinguishes between frontogenesis and frontolysis: positive values indicate front intensification, whereas negative values correspond to front weakening.

$$\mathbf{Q} = \begin{pmatrix} Q_x \\ Q_y \end{pmatrix} = - \begin{pmatrix} u_x b_x + v_x b_y \\ u_y b_x + v_y b_y \end{pmatrix}. \quad (4)$$

The evolution of the rate of change of $|\nabla_H b|$ and advective frontogenetic tendency further suggests that buoyancy gradients are sustained for longer periods in the wave-forced simulations than in the front-only cases, evident from Fig. 6b,c. This persistence, in turn, modulates the subinertial flow timescale. We illustrate this by plotting contours of the envelope of the frontogenetic tendency, which show the gradual evolution of subinertial timescales over the 60-day period in the wave-forced cases. Moreover, increases in M^2 align with the development of the advective frontogenetic tendency. From these experiments, we conclude that the WW case exhibits only weak frontogenesis, whereas the SW case is capable of inducing frontogenesis at a

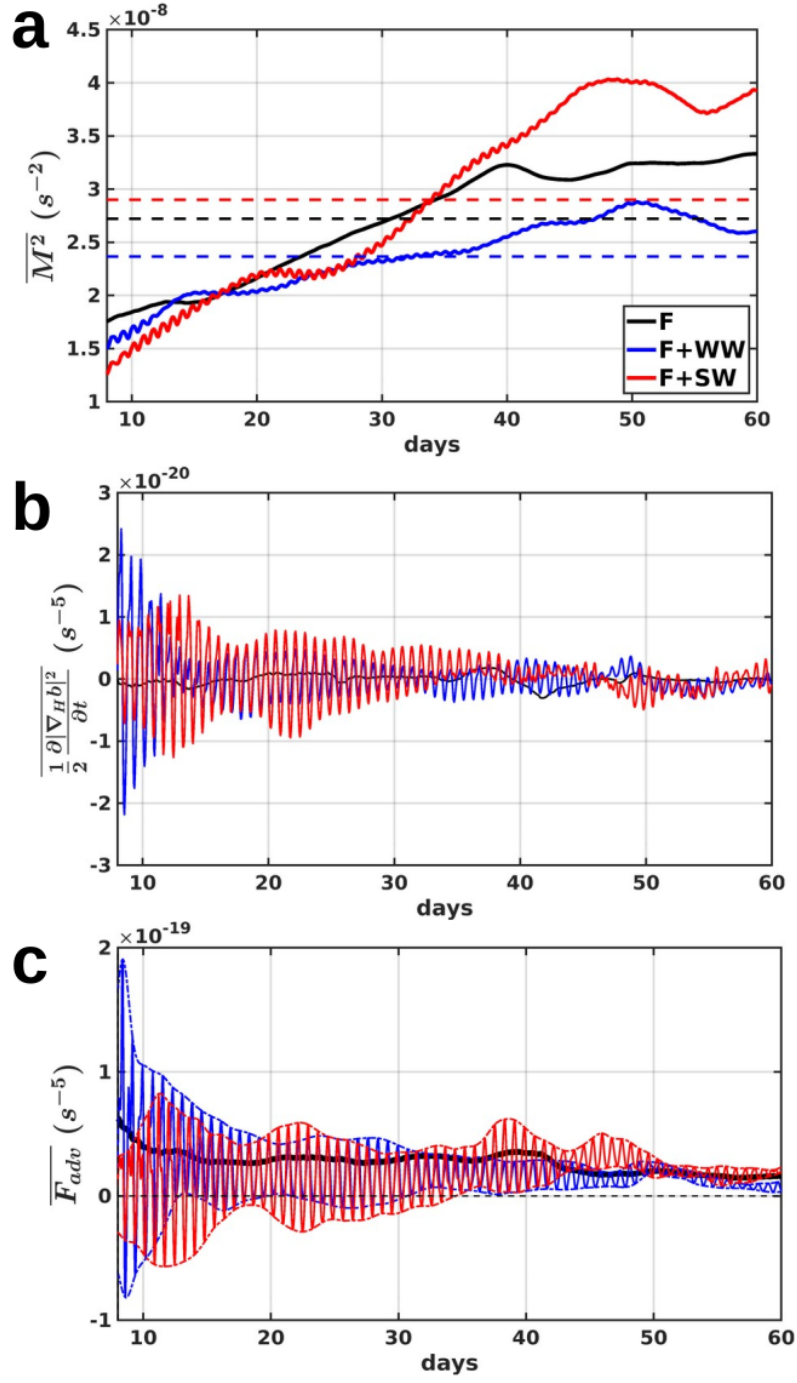


FIG. 6: Domain averaged (a) M^2 , (b) $\frac{1}{2} \frac{\partial^2 |\nabla_H b|^2}{\partial t^2}$, and (c) advective frontogenetic tendency $\overline{F_{adv}}$ over the same period, day 8-60 at 3.5 m depth for the F, F+WW, and F+SW cases. The dashed line in panel (a) represents the average $\overline{M^2}$ over 8-60 days over the domain. The envelope associated with the F is also shown in a dashed line.

later part of the simulation, relative to the F case, beyond 35 days for SW cases, likely via straining mesoscale flow [68].

A key question is how tracers become subducted and what role the phase of the inertial frequency, modified by the background vorticity, plays in subducting tracers from the surface and obducting tracers from below. To address this, we examine the evolution of the flow by studying its impact on vorticity, which is largely governed by

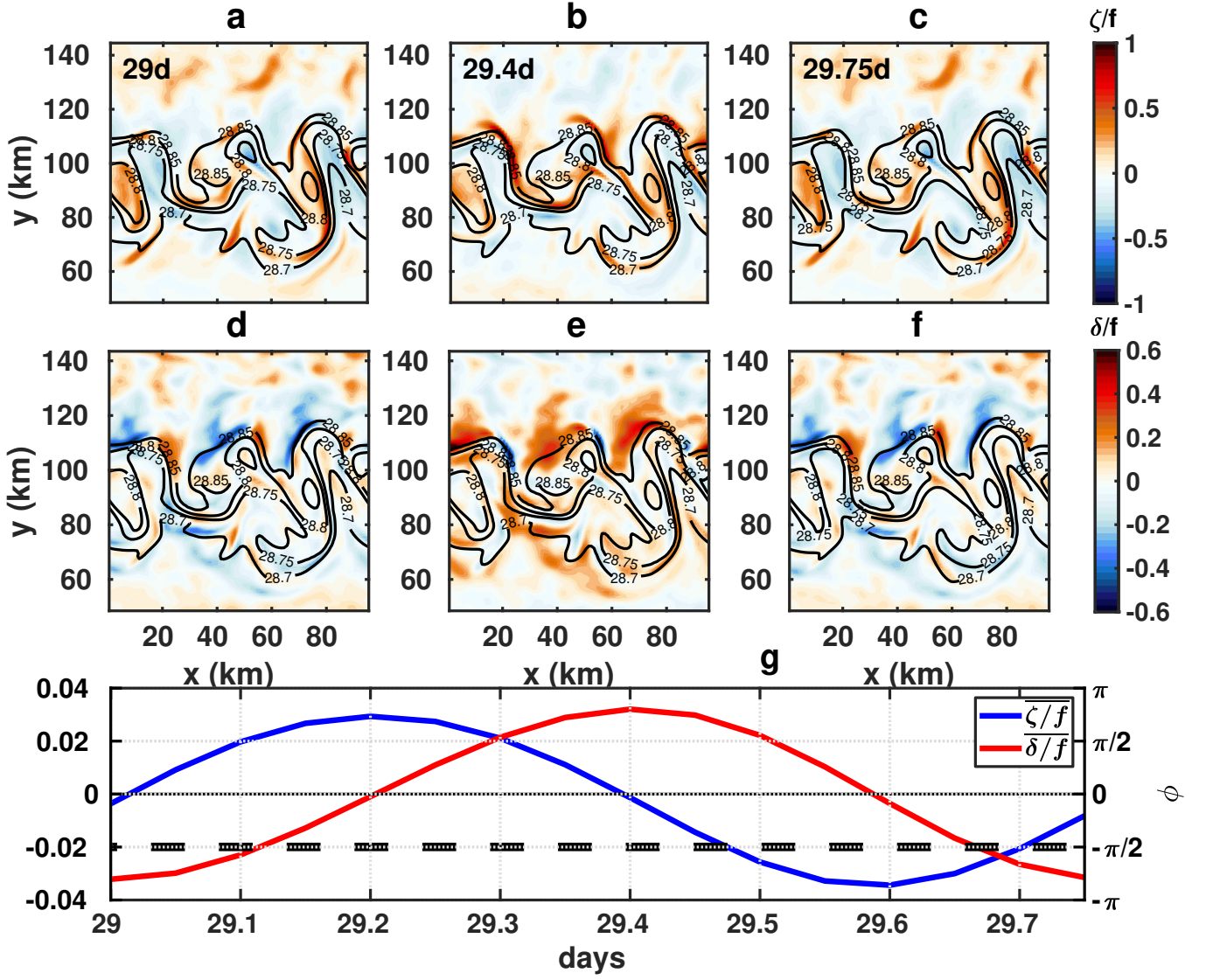


FIG. 7: Panels (a)–(c) and (d)–(f) illustrate the relative vorticity (ζ) and divergence (δ), respectively, normalized by the Coriolis parameter f , at three distinct time steps within an inertial period. These snapshots capture the frontal structure, characterized by intense wave activity at a depth of 3.5 m. The time intervals span from day 29.00 to day 29.75 of the simulation, with 9-hour increments between each. Overlaid contours of potential density anomaly are provided for additional reference. Panel (g) shows the spatially averaged vorticity and divergence, zonally and meridionally averaged over a 48 km region from the north-south boundary, during the inertial period. Also presented is the relative phase difference ϕ in the range $[-\pi, \pi]$ between divergence and vorticity.

$$\frac{D\zeta}{Dt} \approx \underbrace{-\delta(\zeta + f)}_{\text{vortex stretching}} \quad (5)$$

The relative vorticity of the flow modifies the effective NIW frequency as $f_{eff} = f + \frac{\zeta}{2}$ and consequently, a vorticity gradient in the flow induces a phase difference between NIWs in different regions of the flow, leading to convergence and divergence. The divergence is itself modulated by the relative vorticity according to $\partial\delta/\partial t \approx f\zeta$.

When the two velocity vectors are in opposite phases, either directed toward each other or away from each other, the resulting convergence or divergence drives vertical motion within the evolving front. Convergence, where the vectors are directed inward, promotes subduction, while divergence, with the vectors directed outward, favors obduction.

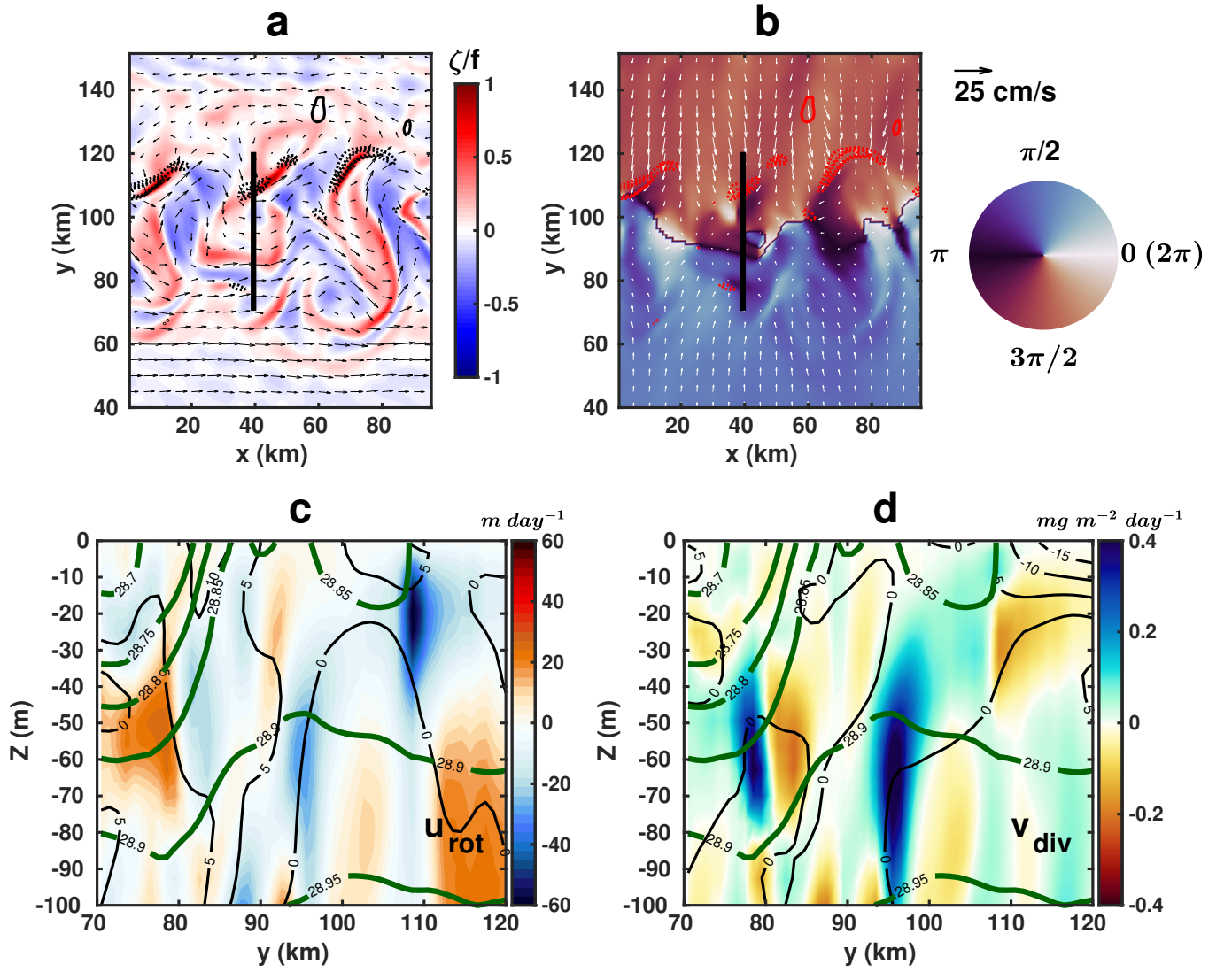


FIG. 8: (a) Relative vorticity with rotational velocity vectors. (b) Phase map of $\theta = \tan^{-1}(v_d/u_d)$, where u_d and v_d are the divergent velocity components, shown on day 31.4 for the F+SW case at 3.5 m. Contours of convergence/divergence ($|\delta/f|$) greater than 0.3 are overlaid, with convergence shown in dotted lines and divergence in dashed lines. (c) Vertical section along the thick black dashed line: rotational zonal velocity (u_{rot} , black contours) and potential density (green contours) with vertical velocity (shading). (d) Vertical tracer fluxes (shading) and the meridional divergent velocity component (v_{div} , black contours) with potential density (green contours), for the upper 100 m.

In what follows, we focus on the strong-wave simulation and track the evolution of the front over one inertial period. As a case study, we illustrate how convergence and divergence emerge and emphasize their role in driving tracer subduction at distinct times within an inertial period.

From the vorticity equation, an enhanced magnitude of the material derivative of relative vorticity, $D\zeta/Dt$, across the cyclonic and anticyclonic eddies induces horizontal convergence, which drives the subduction process. Conversely, the associated divergence favors obduction when $D\zeta/Dt$ is negative. At the front, subduction corresponds to negative vertical velocity, whereas obduction is related to positive vertical velocity. Furthermore, at the submesoscale, for a positive $D\zeta/Dt$, cyclonic eddies induce stronger convergence than anticyclonic eddies. This behavior, as inferred from the expression in Equation 4, which includes the f term added to the relative vorticity, introduces an asymmetry that drives irreversible vertical transport. We illustrate this characterization with a representative example, showing the evolution of vorticity and divergence over an 18-hour inertial period that begins on day 29, in Fig. 7. The domain-averaged material derivative of vorticity and the right-hand side of Equation 4 indicate an approximate balance at 3.5 m depth (SI Fig. S10a, shows days 28–35 for the SW case). Moreover, regions exhibiting stronger $D\zeta/Dt$ are associated with subduction. A coherent correspondence between $D\zeta/Dt$ and the

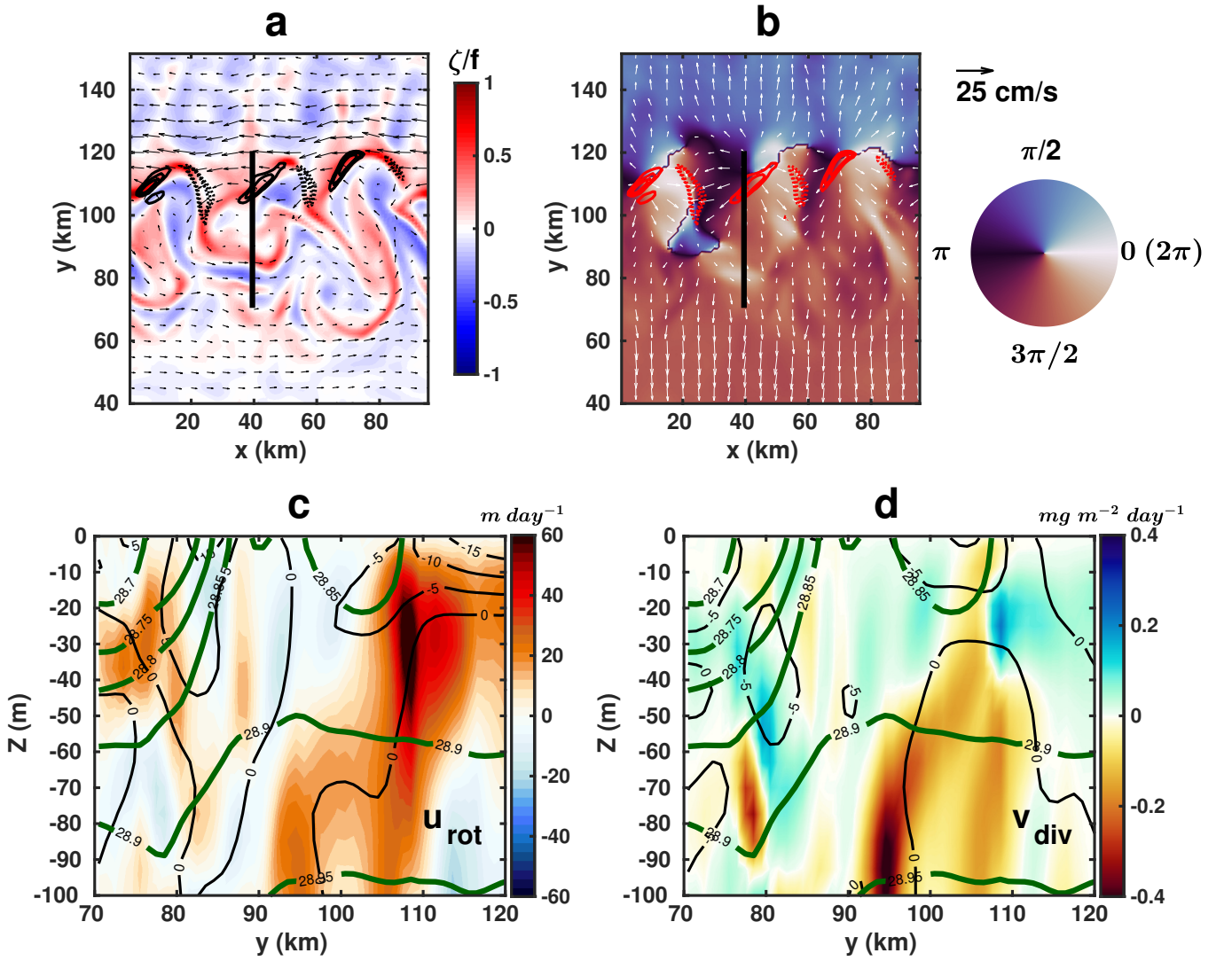


FIG. 9: (a) Relative vorticity with rotational velocity vectors. (b) Phase map of $\theta = \tan^{-1}(v_d/u_d)$, where u_d and v_d are the divergent velocity components, shown on day 31.6 for the F+SW case at 3.5 m within an inertial period. Contours of convergence/divergence ($|\delta/f|$) greater than 0.3 are overlaid, with convergence shown in dotted lines and divergence in dashed lines. (c) Vertical section along the thick black dashed line: rotational zonal velocity (u_{rot} , black contours) and potential density (green contours) with vertical velocity (shading). (d) Vertical tracer fluxes (shading) and the meridional divergent velocity component (v_{div} , black contours) with potential density (green contours), for the upper 100 m.

right-hand side of Equation 4 is evident in the spatial maps shown in SI Fig. S10. b-d and S10. e-g over the interval from 29 to 29.75 days. On average, the vorticity field exhibits a phase lead of $\frac{\pi}{2}$ relative to the divergence signal. This phase relationship reflects the coupling between wave dynamics and the nonlinear evolution of the front under strong near-inertial waves (NIWs), which enhance convergences both within and beneath the mixed layer.

We next examine how subduction occurs during the F+SW scenario by analyzing snapshots of the evolving front at days 31.4 and 31.6 (a 4.8-hour interval). Figs. 8 and 9 illustrate the patterns of convergence and divergence at a depth of 3.5 m (see the caption for reference). The vorticity field and the phase map of the divergent velocity component show that during convergence, the current vectors align toward the front, resulting in enhanced negative vertical velocity and negative tracer covariance fluxes, as observed in the section plotted along the reference line.

However, within the subsequent 4.8 hours, the vectors shift to an opposite phase, leading to divergence and obduction. This state is characterized by positive vertical velocity and positive tracer covariance, though the latter does not necessarily imply net transport. In the following section, we verify and characterize the occurrence of subduction associated with nonlinearity in

the problem and further clarify the underlying dynamics using tracer covariance analysis in frequency–wavenumber space. A representative sequence from this movie is shown in SI Movie S2 for days 28–35, illustrating the convergence and associated subduction in the SW case.

G. Vertical Tracer Covariance

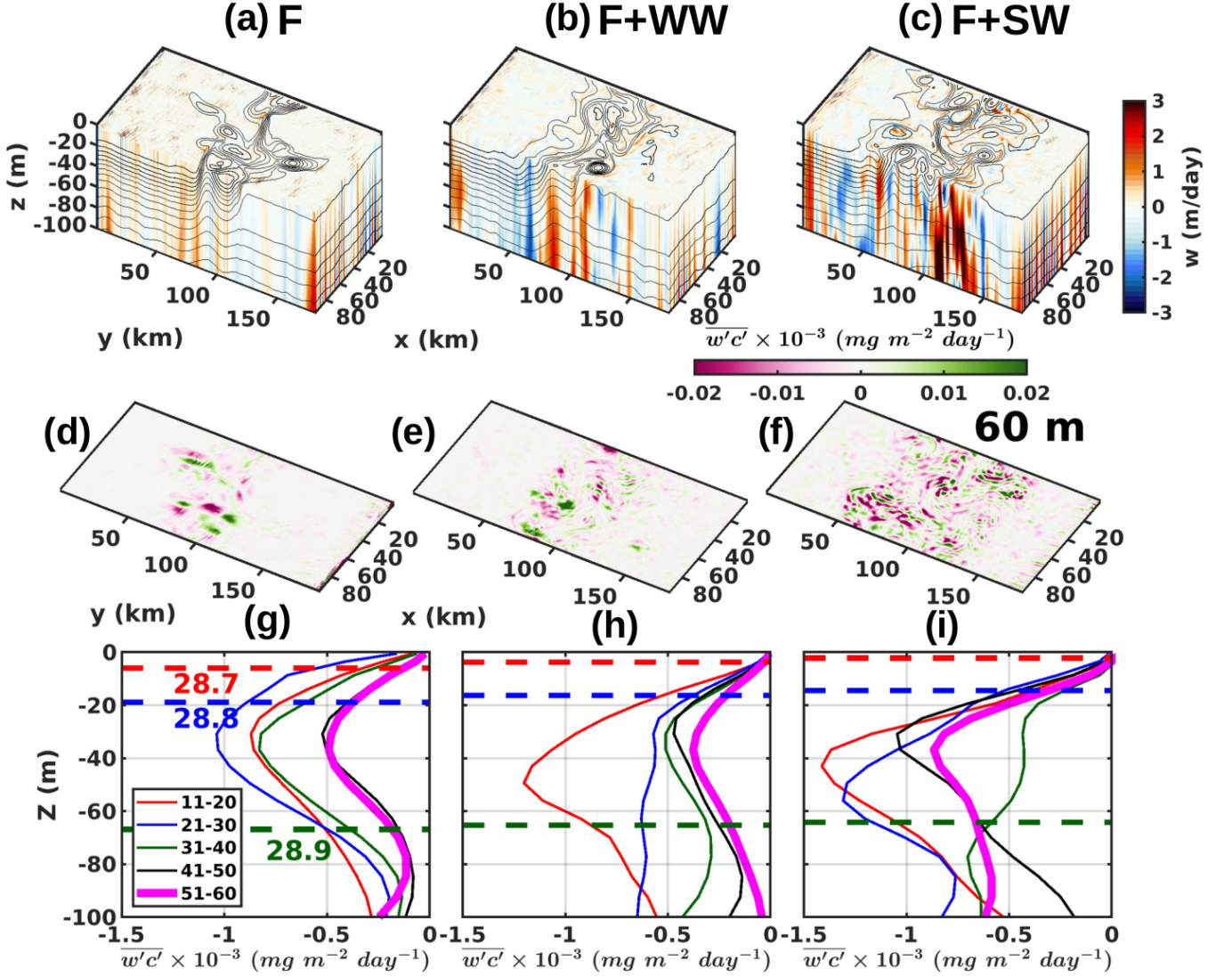


FIG. 10: Panels (a–c) show the vertical velocity averaged over days 51–60 for the upper 100 m (with the upper surface corresponding to -3.5 m), overlaid with contours of potential density anomaly. Panels (d–f) present the tracer covariance fluxes at a depth of 60 m. Panels (g–i) show the 10-day and domain-averaged (in x and y) vertical tracer fluxes as a function of depth, spanning days 11–60 with an interval of 10 days, and the isopycnal depth of 28.7 (red), 28.8 (blue), and 28.9 kg m^{-3} (green) averaged over days 51–60 computed relative to $z = -3.5$ m.

The vertical tracer flux is defined as the product of vertical velocity and tracer concentration anomalies, (w', c') , where anomalies are computed by removing the horizontal area mean. Accordingly, the domain-averaged flux is expressed as $\overline{w'c'} = (\overline{w} - \overline{w_{xy}})(\overline{c} - \overline{c_{xy}})$. The corresponding vertical tracer covariance at depth z_0 is given by

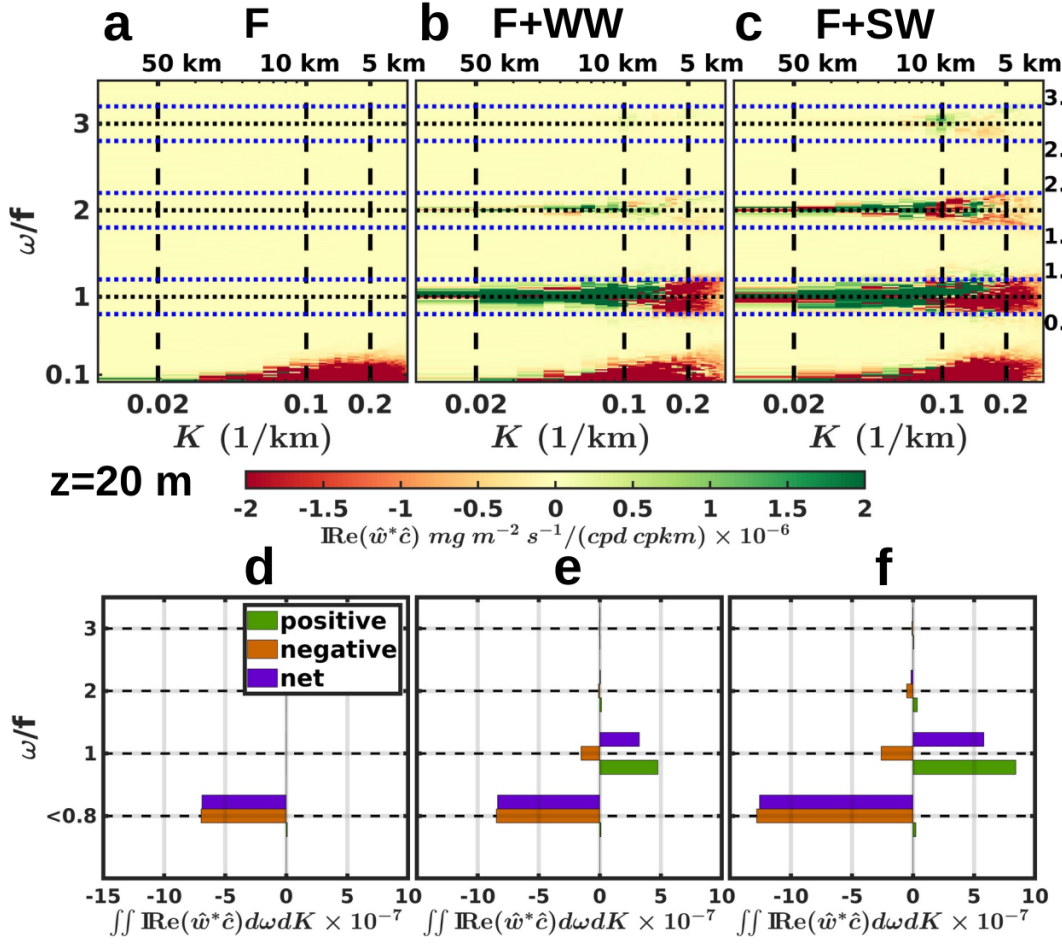


FIG. 11: (a-c) shows the isotropic vertical tracer-covariance spectra of tracer concentration and vertical velocity anomalies (c' ; $mg\ m^{-3}$, w' ; $m\ s^{-1}$) in frequency-wavenumber space ($\omega - K$), where $K = \sqrt{k_x^2 + k_y^2}$, ω is the frequency, k_x , and k_y are the zonal, and meridional wavenumber for the three experiments with F, F+WW, and F+SW, respectively, at a depth of 20 m (within the mixed-layer) from 8 to 60 days. The thin horizontal dotted line in black denotes the Coriolis frequency f and its super-inertial frequencies ($2f$ and $3f$); their bands in the thin blue dotted line correspond to $\pm 0.2f$ about them, respectively. The thin vertical dashed line corresponds to the horizontal scale of 50 km. (d-f) shows the bar graph of integrated power for the frequency range below $0.8f$ (sub-inertial band), between $f \pm 0.2f$ (inertial band), $2f \pm 0.2f$, and $3f \pm 0.2f$ (super-inertial bands) for the positive (green), negative (red), and their net contribution (purple) from the numerical experiments.

$$\overline{w'c'}(z_0) = \frac{1}{TL_xL_y} \int_0^T \int_0^{L_x} \int_0^{L_y} w'(x, y, z_0, t) c'(x, y, z_0, t) dx dy dt \quad (6)$$

$$= \frac{1}{TL_xL_y} \int \int \Re\{\hat{w}^* \hat{c}\}(K, \omega, z_0) dK d\omega. \quad (7)$$

where, T , L_x , and L_y are the temporal duration and horizontal domain extents, $K = \sqrt{k_x^2 + k_y^2}$ is the horizontal wavenumber, and ω is frequency. The vertical tracer covariance spectrum is given by $\Re\{\hat{w}^* \hat{c}\}(K, \omega, z_0)$, with \hat{w} , and \hat{c} denoting the Fourier transform of vertical velocity, tracer concentration anomalies, and the operator $*$ representing the complex conjugate. Before presenting the covariance spectra, we first examine the evolution of vertical velocity at 20 m depth, averaged over the final 10 days of the simulation (≈ 13 inertial periods; Fig. 10a-c). Compared to the front-only case, the mean vertical velocity is larger when waves are included, with the strongest response in the F+SW case. The corresponding tracer fluxes at 60 m depth (Fig. 10d-f) also show enhancement with increasing wave amplitude, particularly in the last 10 days, where the positive (pink) anomalies indicate stronger transport near the mixed layer that diminishes with depth.

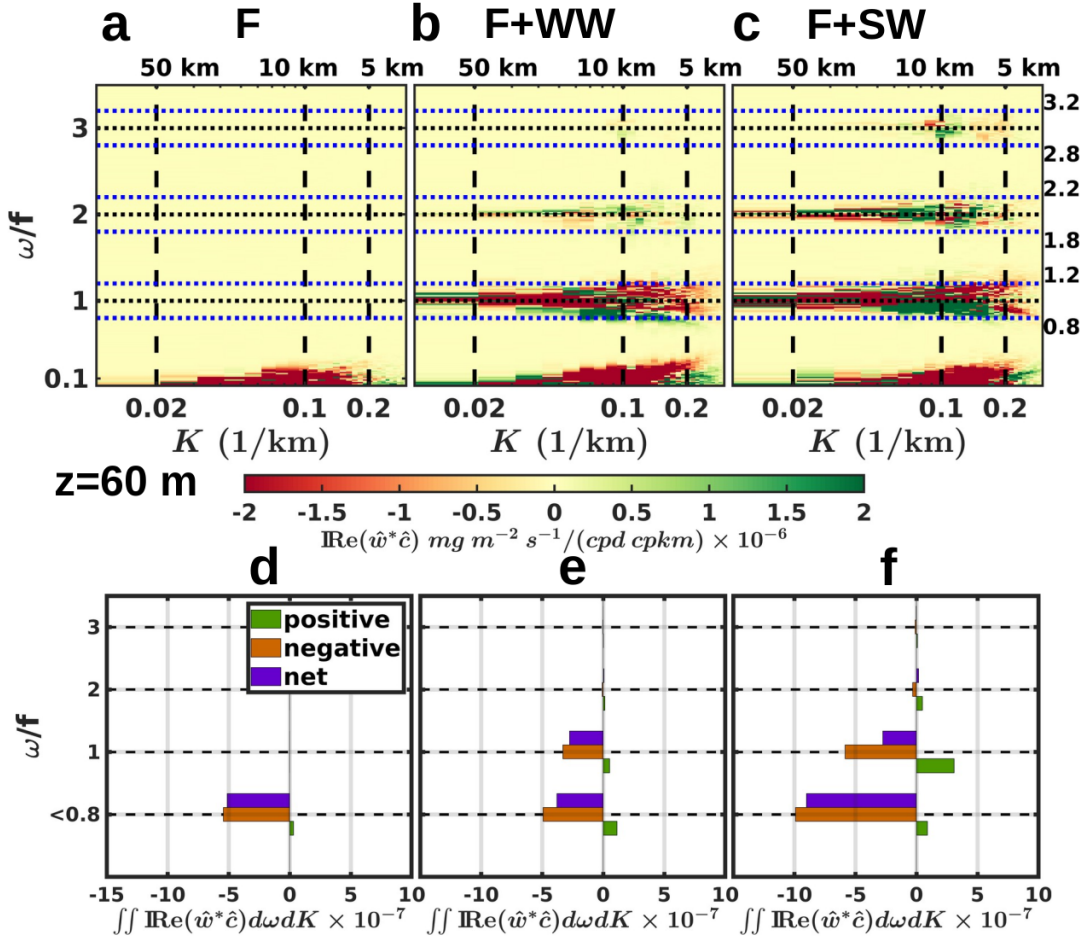


FIG. 12: (a-c) shows the isotropic vertical tracer-covariance spectra of tracer concentration (c' ; mg m^{-3}) and vertical velocity (w' ; m s^{-1}) anomalies in frequency-wavenumber space ($\omega - K$), where $K = \sqrt{k_x^2 + k_y^2}$, ω is the frequency, k_x , and k_y are the zonal, and meridional wavenumber for the three experiments with F, F+WW, and F+SW, respectively at a depth of 60 m (below the mixed-layer) from 8 to 60 days. The thin horizontal dotted line in black denotes the Coriolis frequency f and its super-inertial frequencies ($2f$ and $3f$); their bands in the thin blue dotted line correspond to $\pm 0.2f$ about them, respectively. The thin vertical dashed line corresponds to the horizontal scale of 50 km, 10 km, and 5 km. (d-f) shows the bar graph of integrated power for the frequency range below $0.8f$ (sub-inertial band), between $f \pm 0.2f$ (inertial band), $2f \pm 0.2f$, and $3f \pm 0.2f$ (super-inertial bands) for the positive (green), negative (orange), and their net contribution (purple) from the numerical experiments.

To quantify these patterns, we compute isotropic tracer covariance spectra at 20 m (within the MLD) and 60 m (below the MLD) for all three cases (Figs. 11, 12). Prior to spectral analysis, area means in the meridional direction were removed (excluding 48 km from the boundaries), temporal means were subtracted, and anomalies were tapered with a Tukey window ($r = 0.1$) in space and time. As a convention, negative covariance indicates vertical transport due to subduction of a positive tracer anomaly or abduction of a negative tracer anomaly, whereas positive covariance corresponds to tracer restoration. At 20 m, the front-only case shows predominantly negative covariance in the subinertial band and negligible contribution in the inertial band. When waves are included, the covariance becomes mostly positive at mesoscales, with sign reversals at smaller scales and stronger negative contributions in the super-inertial band as the wave amplitude increases (Fig. S11). Integrated spectra further reveal that net tracer covariance grows with increasing wave amplitude in the subinertial band ($\omega < 0.8f$), while it remains positive in the inertial band ($0.8f < \omega < 1.2f$), indicating little contribution from inertial motions to vertical transport within the MLD.

Below the MLD (60 m depth), all three cases exhibit negative tracer covariance in the subinertial band, with additional positive contributions at higher wavenumbers. In the inertial band, the wave-forced cases show enhanced negative covariance across the mesoscale–submesoscale range, with patches of systematic positive contributions. At super-inertial frequencies, alternating negative and positive patterns emerge, though their integrated effect is small compared to subinertial and inertial frequencies. These results suggest that, below the mixed layer, tracer transport arises from a combination of the background frontal flow and refracted NIWs that interact nonlinearly with submesoscale currents.

IV. CONCLUSIONS

In this study, we investigated the vertical transport of passive tracers in an idealized ocean model, focusing on the influence of near-inertial wind forcing on a density front representative of Balearic Sea conditions during the CALYPSO campaign (February–March 2022). Using simulations at 1 km horizontal resolution with varying NIWs, we found that tracer subduction occurs both within and beneath the mixed layer, with the strongest wave-forced case producing a tracer deficit nearly twice that of the unforced front. PDFs reveal enhanced skewness in vorticity and negative skewness in divergence, consistent at submesoscales. The isopycnal slope exhibits pronounced extrema relative to the F case, indicating that frontogenesis becomes increasingly important—particularly in the later stages of the simulation—and is further enhanced in the strong wave-forced cases.

Spectral analysis of vertical velocity reveals that inertial wind forcing modifies the power distribution across scales, particularly in the subinertial range, with multiple superinertial frequency bands centered at the harmonics of the inertial frequency. Nonlinear transfers emerge in the inertial and superinertial ranges, and tracer flux diagnostics show that subinertial components dominate vertical transport within the mixed layer, increasing with stronger forcing. Below the mixed layer, the tracer fluxes are modified at both the subinertial and inertial frequencies, and the net transport is greater than the transport contributed by fronts. In contrast, high-frequency motions at $2f, 3f, \dots$ contribute little to net transport, as NIWs decay rapidly within the mixed layer, with only a fraction of energy penetrating below.

Our experiments employ idealized viscosity coefficients that do not account for enhanced mixing by near-inertial wave shear, which would likely enhance vertical transport [76]. The results indicate that tracer transport by near-inertial pumping is not entirely reversible and that the waves contribute to tracer transport through the rectification effect in a submesoscale flow.

-
- [1] M. H. Alford, J. A. MacKinnon, H. L. Simmons, and J. D. Nash. Near-inertial internal gravity waves in the ocean. *Annual review of marine science*, 8(1): 95–123, 2016. doi: 10.1146/annurev-marine-010814-015746.
 - [2] D. Balwada, K. S. Smith, and R. Abernathey. Submesoscale vertical velocities enhance tracer subduction in an idealized Antarctic Circumpolar Current. *Geophysical Research Letters*, 45(18):9790–9802, 2018. doi: 10.1029/2018GL079244.
 - [3] D. Balwada, Q. Xiao, S. Smith, R. Abernathey, and A. R. Gray. Vertical fluxes conditioned on vorticity and strain reveal submesoscale ventilation. *Journal of Physical Oceanography*, 51(9):2883–2901, 2021. doi: 10.1175/JPO-D-21-0016.1.
 - [4] R. Barkan, M. J. Molemaker, K. Srinivasan, J. C. McWilliams, and E. A. D’Asaro. The role of horizontal divergence in submesoscale frontogenesis. *Journal of Physical Oceanography*, 49(6):1593–1618, 2019. doi: 10.1175/JPO-D-18-0162.1.
 - [5] J. Callies and R. Ferrari. Interpreting energy and tracer spectra of upper-ocean turbulence in the submesoscale range (1–200 km). *Journal of Physical Oceanography*, 43(11):2456–2474, 2013. doi: 10.1175/JPO-D-13-063.1.
 - [6] J. Callies and W. Wu. Some expectations for submesoscale sea surface height variance spectra. *Journal of Physical Oceanography*, 49(9):2271–2289, 2019. doi: 10.1175/JPO-D-18-0272.1.
 - [7] X. Capet, J. C. McWilliams, M. J. Molemaker, and A. F. Shchepetkin. Mesoscale to submesoscale transition in the California Current System. Part III: Energy balance and flux. *Journal of Physical Oceanography*, 38(10):2256–2269, 2008. doi: 10.1175/2008JPO3810.1.
 - [8] Y. Chen, D. Straub, and L.-P. Nadeau. Interaction of Nonlinear Ekman Pumping, Near-Inertial Oscillations, and Geostrophic Turbulence in an Idealized Coupled Model. *Journal of Physical Oceanography*, 51(3):975–987, 2021. doi: 10.1175/JPO-D-20-0268.1.
 - [9] S. Danilov and D. Gurarie. Scaling, spectra and zonal jets in beta-plane turbulence. *Physics of fluids*, 16(7):2592–2603, 2004. doi: 10.1063/1.1752928.
 - [10] E. D’Asaro, T. M. S. Johnston, A. Mahadevan, A. Pascual, D. L. Rudnick, J. intoré, K. Abbott, J. T. Allen, E. Alou-Font, H. M. Aravind, M. Belgacem, M. Berta, B. Casas, L. R. Centurioni, H. R. Cheslack, E. Cutolo, M. Dever, F. M. Falcieri, J. T. Farrar, M. Freilich, M. Garcia-Jove, G. Gregori, B. Hodges, A. Kinsella, M. Lankhorst, P. Lermusiaux, C. McNeil, L. Middleton, B. Mourre, L. Oms, T. M. Ozgokmen, P.-M. Poulain, I. I. Rypina, U. Send, A. Y. Shcherbina, D. R. Tarry, G. Testa, A. Z. Worden, W. Wu, and N. Zarokanellos. CALYPSO - Coherent Lagrangian Pathways from the Surface Ocean to Interior: Data set. Technical report, Woods Hole Oceanographic Institution, 2025.
 - [11] E. A. D’Asaro. Upper-ocean inertial currents forced by a strong storm. Part II: Modeling. *Journal of physical oceanography*, 25(11):2937–2952, 1995. doi: 10.1175/1520-0485(1995)025<2937:UOICFB>2.0.CO;2.
 - [12] E. A. D’Asaro. Upper-ocean inertial currents forced by a strong storm. Part III: Interaction of inertial currents and mesoscale eddies. *Journal of physical oceanography*, 25(11):2953–2958, 1995. doi: 10.1175/1520-0485(1995)025<2953:UOICFB>2.0.CO;2.
 - [13] E. A. D’Asaro, C. C. Eriksen, M. D. Levine, P. Niiler, P. Van Meurs, et al. Upper-ocean inertial currents forced by a strong storm. Part I: Data and comparisons with linear theory. *Journal of Physical Oceanography*, 25(11):2909–2936, 1995. doi: 10.1175/1520-0485(1995)025<2909:UOICFB>2.0.CO;2.
 - [14] W. Dong, O. Bühler, and K. S. Smith. Geostrophic eddies spread near-inertial wave energy to high frequencies. *Journal of Physical Oceanography*, 53(5): 1311–1322, 2023. doi: 10.1175/JPO-D-22-0153.1.

- [15] D. Durran, J. A. Weyn, and M. Q. Menchaca. Practical considerations for computing dimensional spectra from gridded data. *Monthly Weather Review*, 145(9):3901–3910, 2017. doi: 10.1175/MWR-D-17-0056.1.
- [16] R. M. Errico. Spectra computed from a limited area grid. *Monthly weather review*, 113(9):1554–1562, 1985. doi: 10.1175/1520-0493(1985)113<1554:SCFALA>2.0.CO;2.
- [17] G. Esposito, S. Donnet, M. Berta, A. Y. Shcherbina, M. Freilich, L. Centurioni, E. A. D’Asaro, J. T. Farrar, T. S. Johnston, A. Mahadevan, et al. Inertial oscillations and frontal processes in an Alboran Sea jet: Effects on divergence and vertical transport. *Journal of Geophysical Research: Oceans*, 128(3):e2022JC019004, 2023. doi: 10.1029/2022JC019004.
- [18] R. Ferrari and C. Wunsch. Ocean circulation kinetic energy: Reservoirs, sources, and sinks. *Annual Review of Fluid Mechanics*, 41(1):253–282, 2009. doi: 10.1146/annurev.fluid.40.111406.102139.
- [19] M. Freilich and A. Mahadevan. Coherent pathways for subduction from the surface mixed layer at ocean fronts. *Journal of Geophysical Research: Oceans*, 126(5):e2020JC017042, 2021. doi: 10.1029/2020JC017042.
- [20] M. A. Freilich and A. Mahadevan. Decomposition of vertical velocity for nutrient transport in the upper ocean. *Journal of Physical Oceanography*, 49(6):1561–1575, 2019. doi: 10.1175/JPO-D-19-0002.1.
- [21] K. Gage and G. Nastrom. On the spectrum of atmospheric velocity fluctuations seen by MST/ST radar and their interpretation. *Radio Science*, 20(6):1339–1347, 1985. doi: 10.1029/RS020i006p01339.
- [22] A. E. Gill. *Atmosphere—ocean dynamics*. Elsevier, 2016.
- [23] J. He and A. Mahadevan. How the source depth of coastal upwelling relates to stratification and wind. *Journal of Geophysical Research: Oceans*, 126(12):e2021JC017621, 2021. doi: 10.1029/2021JC017621.
- [24] B. J. Hoskins. The mathematical theory of frontogenesis. *Annual review of fluid mechanics*, 14(1):131–151, 1982. doi: 10.1146/annurev.fl.14.010182.001023.
- [25] B. J. Hoskins, I. Draghici, and H. Davies. A new look at the ω -equation. *Quarterly Journal of the Royal Meteorological Society*, 104(439):31–38, 1978. doi: 10.1002/qj.49710443903.
- [26] C. S. Jones, Q. Xiao, R. P. Abernathey, and K. S. Smith. Using lagrangian filtering to remove waves from the ocean surface velocity field. *Journal of Advances in Modeling Earth Systems*, 15(4):e2022MS003220, 2023.
- [27] Y. Kawaguchi, T. Wagawa, and Y. Igeta. Near-inertial internal waves and multiple-inertial oscillations trapped by negative vorticity anomaly in the central Sea of Japan. *Progress in Oceanography*, 181:102240, 2020. doi: 10.1016/j.pocean.2019.102240.
- [28] S. M. Kelly. The vertical mode decomposition of surface and internal tides in the presence of a free surface and arbitrary topography. *Journal of Physical Oceanography*, 46(12):3777–3788, 2016. doi: 10.1175/JPO-D-16-0131.1.
- [29] S. M. Kelly, N. L. Jones, G. N. Ivey, and R. J. Lowe. Internal-tide spectroscopy and prediction in the Timor Sea. *Journal of Physical Oceanography*, 45(1):64–83, 2015. doi: 10.1175/JPO-D-14-0007.1.
- [30] P. K. Kundu. A two-dimensional model of inertial oscillations generated by a propagating wind field. *Journal of physical oceanography*, 16(8):1399–1411, 1986. doi: 10.1175/1520-0485(1986)016<1399:ATDMOI>2.0.CO;2.
- [31] E. Kunze. Near-inertial wave propagation in geostrophic shear. *Journal of Physical Oceanography*, 15(5):544–565, 1985. doi: 10.1175/1520-0485(1985)015<0544:NIWPIG>2.0.CO;2.
- [32] R.-C. Lien and P. Müller. Normal-mode decomposition of small-scale oceanic motions. *Journal of physical oceanography*, 22(12):1583–1595, 1992. doi: 10.1175/1520-0485(1992)022<1583:NMDOSS>2.0.CO;2.
- [33] A. Mahadevan. The impact of submesoscale physics on primary productivity of plankton. *Annual review of marine science*, 8(1):161–184, 2016. doi: 10.1146/annurev-marine-010814-015912.
- [34] A. Mahadevan and D. Archer. Modeling the impact of fronts and mesoscale circulation on the nutrient supply and biogeochemistry of the upper ocean. *Journal of Geophysical Research: Oceans*, 105(C1):1209–1225, 2000. doi: 10.1029/1999JC900216.
- [35] A. Mahadevan and J. Campbell. Biogeochemical patchiness at the sea surface. *Geophysical Research Letters*, 29(19):32–1, 2002. doi: 10.1029/2001GL014116.
- [36] A. Mahadevan, J. Oliger, and R. Street. A nonhydrostatic mesoscale ocean model. Part I: Well-posedness and scaling. *Journal of Physical Oceanography*, 26(9):1868–1880, 1996. doi: 10.1175/1520-0485(1996)026<1868:ANMOMP>2.0.CO;2.
- [37] A. Mahadevan, J. Oliger, and R. Street. A nonhydrostatic mesoscale ocean model. Part II: Numerical implementation. *Journal of Physical Oceanography*, 26(9):1881–1900, 1996. doi: 10.1175/1520-0485(1996)026<1881:ANMOMP>2.0.CO;2.
- [38] A. Mahadevan, A. Tandon, and R. Ferrari. Rapid changes in mixed layer stratification driven by submesoscale instabilities and winds. *Journal of Geophysical Research: Oceans*, 115(C3), 2010. doi: 10.1029/2008JC005203.
- [39] M. Maltrud and G. Vallis. Energy spectra and coherent structures in forced two-dimensional and beta-plane turbulence. *Journal of Fluid Mechanics*, 228:321–342, 1991. doi: 10.1017/S0022112091002720.
- [40] E. Mason and A. Pascual. Multiscale variability in the Balearic Sea: An altimetric perspective. *Journal of Geophysical Research: Oceans*, 118(6):3007–3025, 2013. doi: 10.1002/jgrc.20234.
- [41] J. C. McWilliams. Submesoscale currents in the ocean. *Proceedings of the Royal Society A: Mathematical, Physical and Engineering Sciences*, 472(2189):20160117, 2016. doi: 10.1098/rspa.2016.0117.
- [42] M. Müller, B. K. Arbic, J. G. Richman, J. F. Shriver, E. L. Kunze, R. B. Scott, A. J. Wallcraft, and L. Zamudio. Toward an internal gravity wave spectrum in global ocean models. *Geophysical Research Letters*, 42(9):3474–3481, 2015. doi: 10.1002/2015GL063365.
- [43] P. Müller, G. Holloway, F. Henyey, and N. Pomphrey. Nonlinear interactions among internal gravity waves. *Reviews of Geophysics*, 24(3):493–536, 1986. doi: 10.1029/RG024i003p00493.
- [44] T. Nagai, N. Gruber, H. Frenzel, Z. Lachkar, J. C. McWilliams, and G.-K. Plattner. Dominant role of eddies and filaments in the offshore transport of carbon and nutrients in the California Current System. *Journal of Geophysical Research: Oceans*, 120(8):5318–5341, 2015. doi: 10.1002/2015JC010889.
- [45] T. Nagai, A. Tandon, E. Kunze, and A. Mahadevan. Spontaneous generation of near-inertial waves by the kuroshio front. *Journal of Physical Oceanography*, 45(9):2381–2406, 2015.
- [46] P. P. Niiler. On the ekman divergence in an oceanic jet. *Journal of Geophysical Research*, 74(28):7048–7052, 1969.
- [47] D. Olbers and C. Eden. A closure for internal wave–mean flow interaction. Part I: Energy conversion. *Journal of Physical Oceanography*, 47(6):1389–1401, 2017. doi: 10.1175/JPO-D-16-0054.1.
- [48] N. Paul, J. Sukhatme, D. Sengupta, and B. Gayen. Eddy induced trapping and homogenization of freshwater in the Bay of Bengal. *Journal of Geophysical Research: Oceans*, 126(6):e2021JC017180, 2021. doi: 10.1029/2021JC017180.

- [49] N. Paul, J. Sukhatme, B. Gayen, and D. Sengupta. Eddy-Freshwater Interaction Using Regional Ocean Modeling System in the Bay of Bengal. *Journal of Geophysical Research: Oceans*, 128(4):e2022JC019439, 2023. doi: 10.1029/2022JC019439.
- [50] H. T. Pham, V. Verma, S. Sarkar, A. Y. Shcherbina, and E. A. D’Asaro. Rapid downwelling of tracer particles across the boundary layer and into the pycnocline at submesoscale ocean fronts. *Geophysical Research Letters*, 51(17):e2024GL109674, 2024. doi: 10.1029/2024GL109674.
- [51] R. T. Pollard. On the generation by winds of inertial waves in the ocean. In *Deep Sea Research and Oceanographic Abstracts*, volume 17, pages 795–812. Elsevier, 1970. doi: 10.1016/0011-7471(70)90042-2.
- [52] R. T. Pollard and L. A. Regier. Vorticity and vertical circulation at an ocean front. *Journal of Physical Oceanography*, 22(6):609–625, 1992. doi: 1520-0485(1992)022(0609:VAVCAA)2.0.CO;2.
- [53] J. A. Polton, D. M. Lewis, and S. E. Belcher. The role of wave-induced Coriolis–Stokes forcing on the wind-driven mixed layer. *Journal of Physical Oceanography*, 35(4):444–457, 2005. doi: 10.1175/JPO2701.1.
- [54] K. L. Polzin. Mesoscale eddy–internal wave coupling. Part I: Symmetry, wave capture, and results from the Mid-Ocean Dynamics Experiment. *Journal of physical oceanography*, 38(11):2556–2574, 2008. doi: 10.1175/2008JPO3666.1.
- [55] K. L. Polzin. Mesoscale eddy–internal wave coupling. Part II: Energetics and results from PolyMode. *Journal of physical oceanography*, 40(4):789–801, 2010. doi: 10.1175/2009JPO4039.1.
- [56] K. L. Polzin, A. C. Naveira Garabato, T. N. Huussen, B. M. Sloyan, and S. Waterman. Finescale parameterizations of turbulent dissipation. *Journal of Geophysical Research: Oceans*, 119(2):1383–1419, 2014. doi: 10.1002/2013JC008979.
- [57] K. J. Raja, M. C. Buijsman, J. F. Shriver, B. K. Arbic, and O. Siyanbola. Near-inertial wave energetics modulated by background flows in a global model simulation. *Journal of Physical Oceanography*, 52(5):823–840, 2022. doi: 10.1175/JPO-D-21-0130.1.
- [58] R. Samelson and D. Chapman. Evolution of the instability of a mixed-layer front. *Journal of Geophysical Research: Oceans*, 100(C4):6743–6759, 1995. doi: 10.1029/94JC03216.
- [59] R. Samelson and J. Farrar. Models of the sea-surface height expression of the internal-wave continuum. *Journal of Physical Oceanography*, 2024. doi: 10.1175/JPO-D-23-0178.1.
- [60] A. C. Savage, B. K. Arbic, M. H. Alford, J. K. Ansong, J. T. Farrar, D. Menemenlis, A. K. O’Rourke, J. G. Richman, J. F. Shriver, G. Voet, et al. Spectral decomposition of internal gravity wave sea surface height in global models. *Journal of Geophysical Research: Oceans*, 122(10):7803–7821, 2017. doi: 10.1002/2017JC013009.
- [61] M. Shaham and R. Barkan. Spectral flux decomposition in a wind-driven channel flow with near-inertial waves. *Journal of Advances in Modeling Earth Systems*, 17(1):e2023MS004036, 2025. doi: 10.1029/2023MS004036.
- [62] A. Y. Shcherbina, E. A. D’Asaro, C. M. Lee, J. M. Klymak, M. J. Molemaker, and J. C. McWilliams. Statistics of vertical vorticity, divergence, and strain in a developed submesoscale turbulence field. *Geophysical Research Letters*, 40(17):4706–4711, 2013. doi: 10.1002/grl.50919.
- [63] M. A. Spall. Frontogenesis, subduction, and cross-front exchange at upper ocean fronts. *Journal of Geophysical Research: Oceans*, 100(C2):2543–2557, 1995. doi: 10.1029/94JC02860.
- [64] M. E. Stern. Interaction of a uniform wind stress with a geostrophic vortex. In *Deep Sea Research and Oceanographic Abstracts*, volume 12, pages 355–367. Elsevier, 1965. doi: 10.1016/0011-7471(65)90007-0.
- [65] J. Thomas. Turbulent wave-balance exchanges in the ocean. *Proceedings of the Royal Society A*, 479(2276):20220565, 2023. doi: 10.1098/rspa.2022.0565.
- [66] J. Thomas and D. Daniel. Turbulent exchanges between near-inertial waves and balanced flows. *Journal of Fluid Mechanics*, 902:A7, 2020. doi: 10.1017/jfm.2020.510.
- [67] L. Thomas and R. Ferrari. Friction, frontogenesis, and the stratification of the surface mixed layer. *Journal of Physical Oceanography*, 38(11):2501–2518, 2008. doi: 10.1175/2008JPO3797.1.
- [68] L. N. Thomas. On the effects of frontogenetic strain on symmetric instability and inertia–gravity waves. *Journal of Fluid Mechanics*, 711:620–640, 2012. doi: 10.1017/jfm.2012.416.
- [69] L. N. Thomas and C. M. Lee. Intensification of ocean fronts by down-front winds. *Journal of Physical Oceanography*, 35(6):1086–1102, 2005.
- [70] H. Torres, P. Klein, L. Siegelman, B. Qiu, S. Chen, C. Ubelmann, J. Wang, D. Menemenlis, and L.-L. Fu. Diagnosing ocean-wave-turbulence interactions from space. *Geophysical Research Letters*, 46(15):8933–8942, 2019. doi: 10.1029/2019GL083675.
- [71] H. S. Torres, P. Klein, D. Menemenlis, B. Qiu, Z. Su, J. Wang, S. Chen, and L.-L. Fu. Partitioning ocean motions into balanced motions and internal gravity waves: A modeling study in anticipation of future space missions. *Journal of Geophysical Research: Oceans*, 123(11):8084–8105, 2018.
- [72] H. S. Torres, P. Klein, E. D’Asaro, J. Wang, A. F. Thompson, L. Siegelman, D. Menemenlis, E. Rodriguez, A. Wineteer, and D. Perkovic-Martin. Separating energetic internal gravity waves and small-scale frontal dynamics. *Geophysical Research Letters*, 49(6):e2021GL096249, 2022. doi: 10.1029/2021GL096249.
- [73] J. Vanneste. Balance and spontaneous wave generation in geophysical flows. *Annual Review of Fluid Mechanics*, 45(1):147–172, 2013.
- [74] M. Vargas-Yáñez, F. Moya, R. Balbín, R. Santiago, E. Ballesteros, R. F. Sanchez-Leal, P. Romero, and M. C. García-Martínez. Seasonal and long-term variability of the mixed layer depth and its influence on ocean productivity in the Spanish Gulf of Cádiz and Mediterranean Sea. *Frontiers in Marine Science*, 9:901893, 2022. doi: 10.3389/fmars.2022.901893.
- [75] D.-P. Wang. Model of frontogenesis: Subduction and upwelling. *Journal of Marine Research*, 1993. doi: 10.1357/0022240933224034.
- [76] H. Wang, Z. Chen, Z. Zhang, S. Peng, Z. Chen, S. Cai. Parameterization of near-inertial waves induced mixing under the influence of mesoscale eddies. *Journal of Geophysical Research: Oceans*, 130(8):e2025JC022513, 2025. doi: 10.1029/2025JC022513.
- [77] D. B. Whitt and L. N. Thomas. Near-inertial waves in strongly baroclinic currents. *Journal of Physical Oceanography*, 43(4):706–725, 2013. doi: 10.1175/JPO-D-12-0132.1.
- [78] C. Wunsch and R. Ferrari. Vertical mixing, energy, and the general circulation of the oceans. *Annu. Rev. Fluid Mech.*, 36(1):281–314, 2004. doi: 10.1146/annurev.fluid.36.050802.122121.
- [79] L. Yang, R. Barkan, K. Srinivasan, J. C. McWilliams, C. J. Shakespeare, and A. H. Gibson. Oceanic eddies induce a rapid formation of an internal wave continuum. *Communications Earth & Environment*, 4(1):484, 2023. doi: 10.1038/s43247-023-01137-1.
- [80] W. Young and M. B. Jelloul. Propagation of near-inertial oscillations through a geostrophic flow. *Journal of Marine Research*, 1997. doi: 10.1357/0022240973224283.
- [81] W. Zhang and C. L. Wolfe. On the vertical structure of oceanic mesoscale tracer diffusivities. *Journal of Advances in Modeling Earth Systems*, 14(6):e2021MS002891, 2022. doi: 10.1029/2021MS002891.

Open Research

The PSOM model configuration can be found at the GitHub repository (<https://github.com/niharpaul/PSOM-NIWs-CALYPSO---JPO-2025>), datasets, and analysis code associated with the Figures used are available at Zenodo (<http://doi.org/10.5281/zenodo.14279472>). Additionally, the three-dimensional data can be shared upon request to the corresponding author. The authors declare no conflicts of interest, and the results have not been previously published in any journal.

Acknowledgments

This research contributes to the Coherent Lagrangian Pathways from the Surface Ocean to the Interior (CALYPSO) Department Research Initiative, supported by the US Office of Naval Research (ONR). NP acknowledges support from the National Aeronautics and Space Administration (NASA) Sub-Mesoscale Ocean Dynamics Experiment (SMODE) mission through Dr. J. Thomas Farrar. NP gratefully thanks Dr. J. Thomas Farrar, Dr. Eric D'Asaro, Dr. Michael Spall, Dr. Jai Sukhatme, and Dr. Dipanjan Chaudhuri for their valuable feedback and discussion on the analysis. The authors also acknowledge the attendees who provided comments on the poster presented at the 2024 Ocean Sciences Meeting, the 2024 Gordon Research Conference, and the 2025 Ocean Transport and Eddy Energy Climate Process Team (CPT) meeting at the Courant Institute of Mathematical Sciences, New York University, US.

Supplementary Information

1. Figures S1 to S11.
2. Tables S1.
3. Movies S1, and S2.
4. SI text S1, S2, and S3

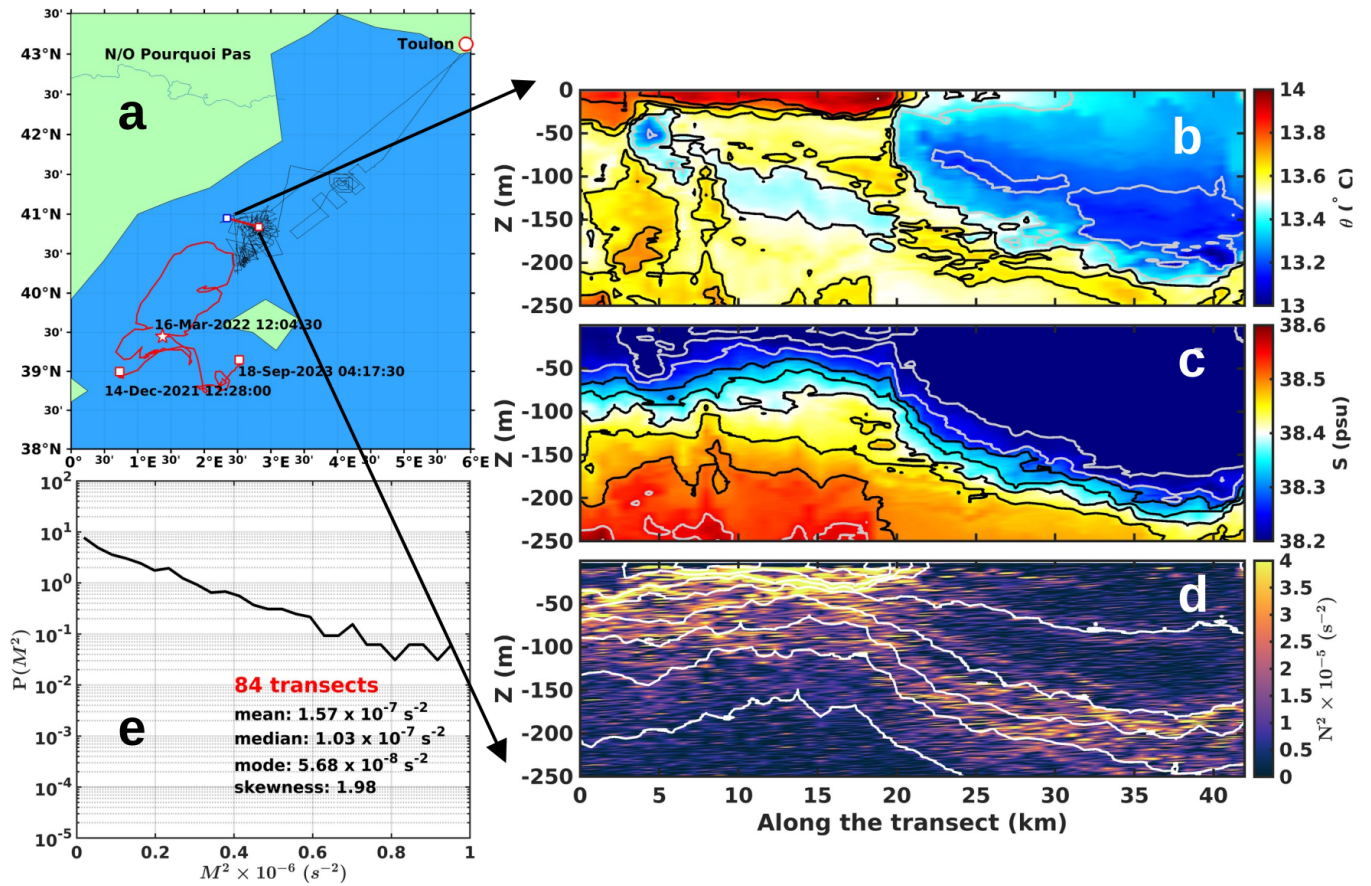


Fig. S1: (a) Survey of the vessel *N/O Pourquoi Pas* conducted in the Balearic Sea from February to March 2022. The trajectory of the ARGO float is also shown, spanning December 14, 2021, to September 18, 2023. (b-d) Potential temperature (θ , °C), salinity (S , psu), and squared Brunt-Väisälä frequency (N^2 , s⁻²) with contours of potential density anomaly (σ_θ , kg m⁻³) across the mesoscale front along the transect highlighted in red in (a). (e) Probability density function of M^2 , defined as $|\nabla_H b|$, at the surface from 84 transects, where b is buoyancy.

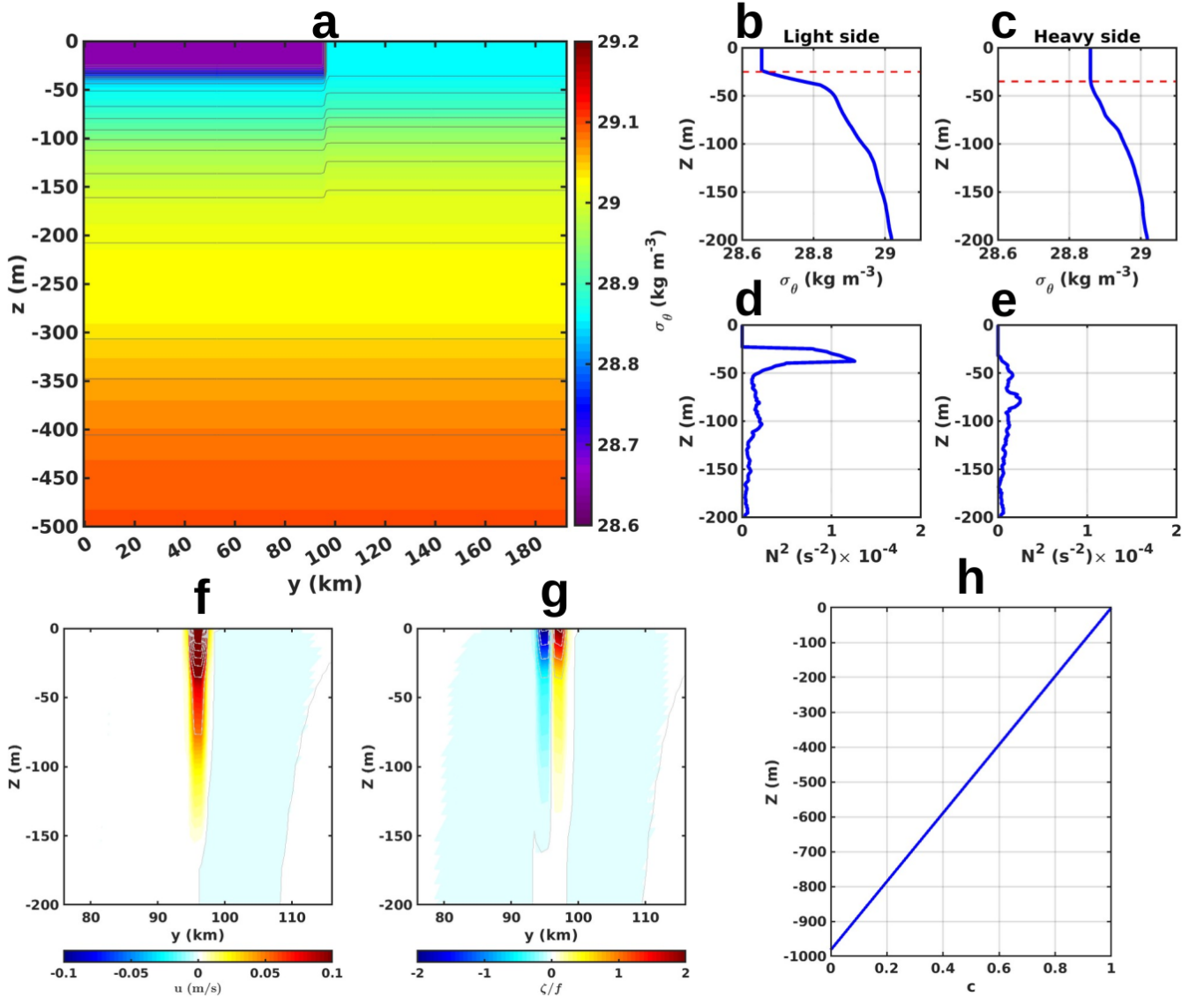


Fig. S2: (a) Potential density anomaly (σ_θ) of the front associated with the transect shown in Fig. S1 (upper 500 m). (b–e) σ_θ and squared Brunt–Väisälä frequency (N^2) with tightness = 0.4, $M^2 = 9.023 \times 10^{-7} \text{ s}^{-2}$, and $M^2/f^2 = 101.13$, where f is the Coriolis parameter. Red dashed lines indicate the mixed layer depths on the light (25 m) and heavy (35 m) sides of the front. (f–h) Initial conditions: zonal velocity u (m s^{-1}), Rossby number ζ/f in the upper 200 m, and a linear tracer profile c (mg m^{-3}) versus depth, varying from 0 at the bottom to 1 at the surface.

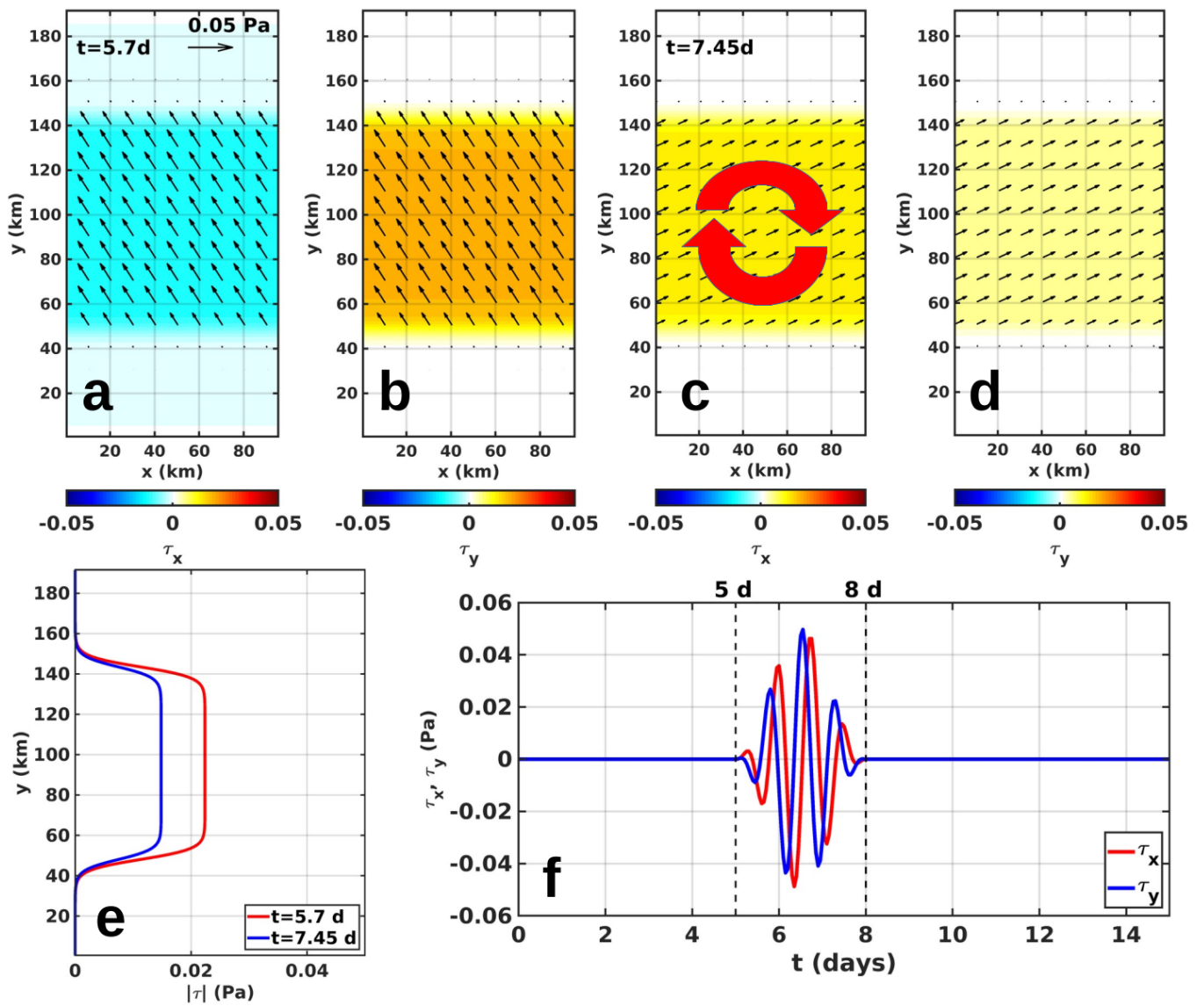


Fig. S3: (a,b) and (c,d) show spatial maps of zonal and meridional wind stress with quivers (τ_x , τ_y) at $t = 5.7$ days and $t = 7.45$ days, respectively. (e) shows the meridional profile of wind stress magnitude corresponding to the times shown in (a–d). (f) presents the 15-day time series of surface wind stress (τ_x , τ_y) at the domain center. Winds are switched on and off between days 5–8 to generate near-inertial waves (NIWs). Clockwise arrows in (c) indicate the rotation direction of the inertial winds.

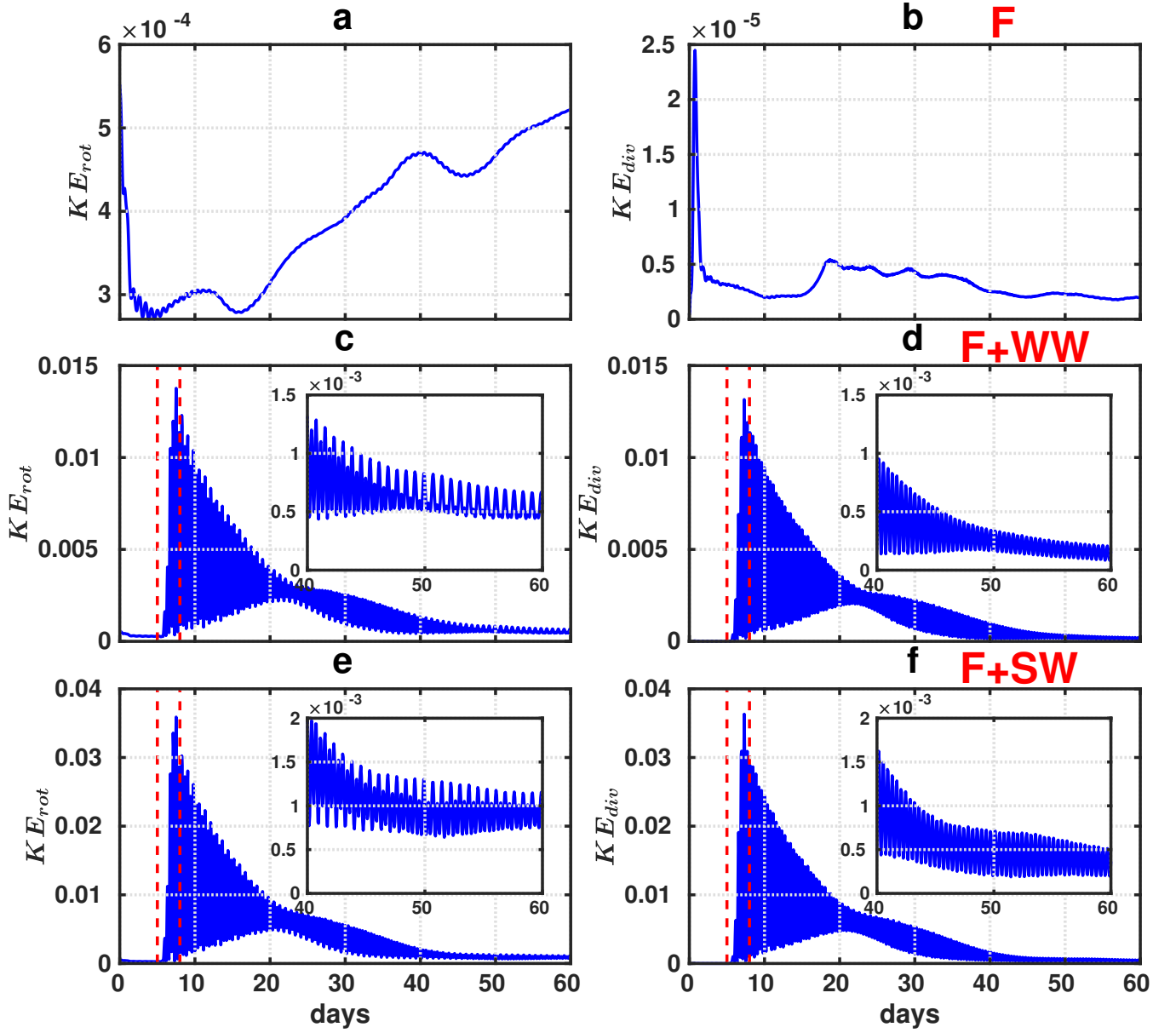


Fig. S4: Columns (a), (c), and (e) display the rotational kinetic energy (KE_{rot}), while columns (b), (d), and (f) represent the divergent kinetic energy (KE_{div}) for the Front (F) and the front with weak and strong waves (F+WW, F+SW) at a depth of 3.5 m throughout the 60-day simulation. Insets in panels (c)–(f) highlight the corresponding kinetic energy between days 40–60 of the simulation. Vertical dashed lines in panels 2 and 3 indicate days 5 and 8, respectively.

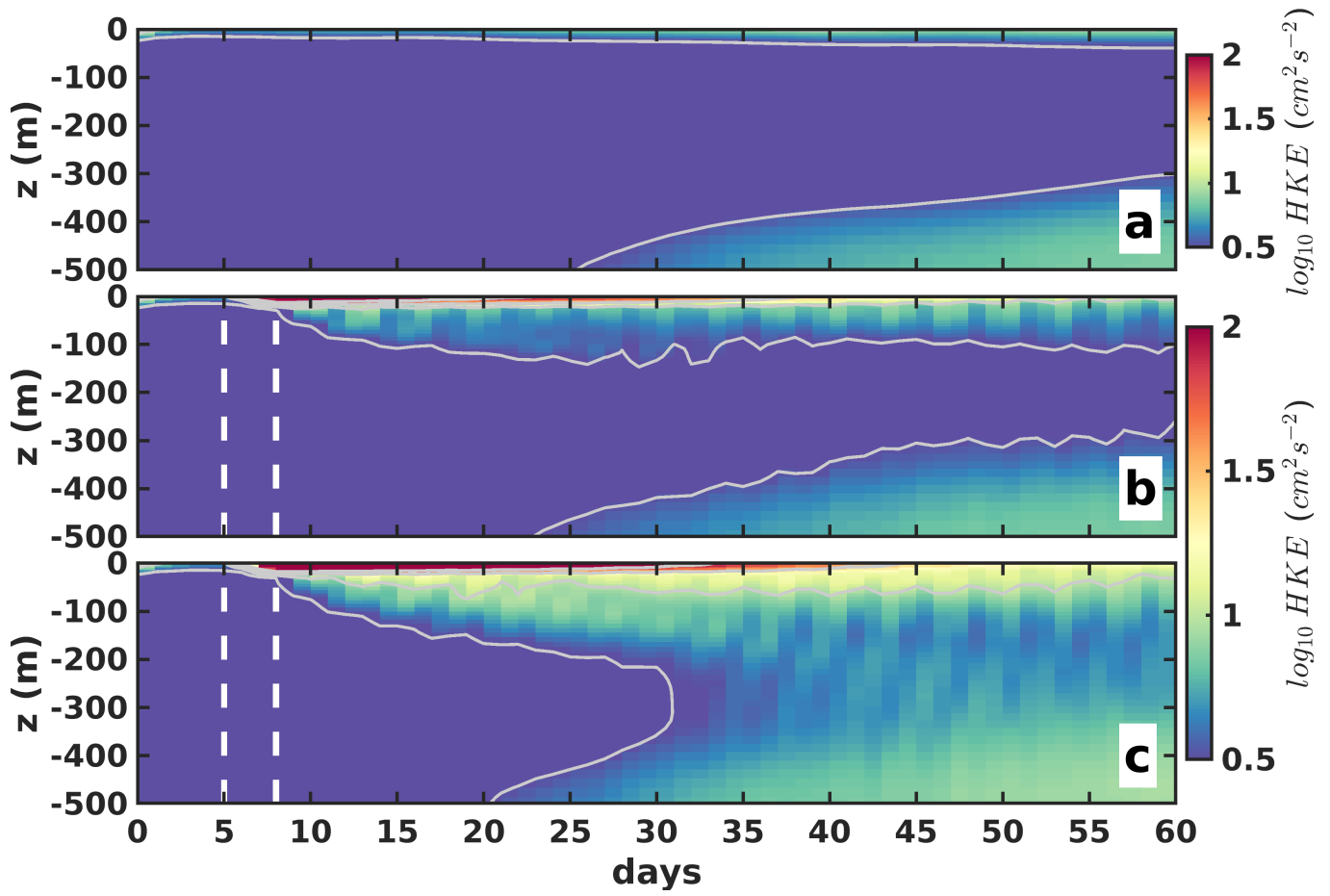


Fig. S5: (a), (b), (c) shows the Hövmöller of average of horizontal kinetic energy (HKE) over the domain at per with the region of isospectra of the front (F), front with weak wave (F+WW), and strong wave cases (F+SW) for the upper 500 m . The white vertical dashed line shows the turning on (day 5) and off period (day 8) of the inertial wind.

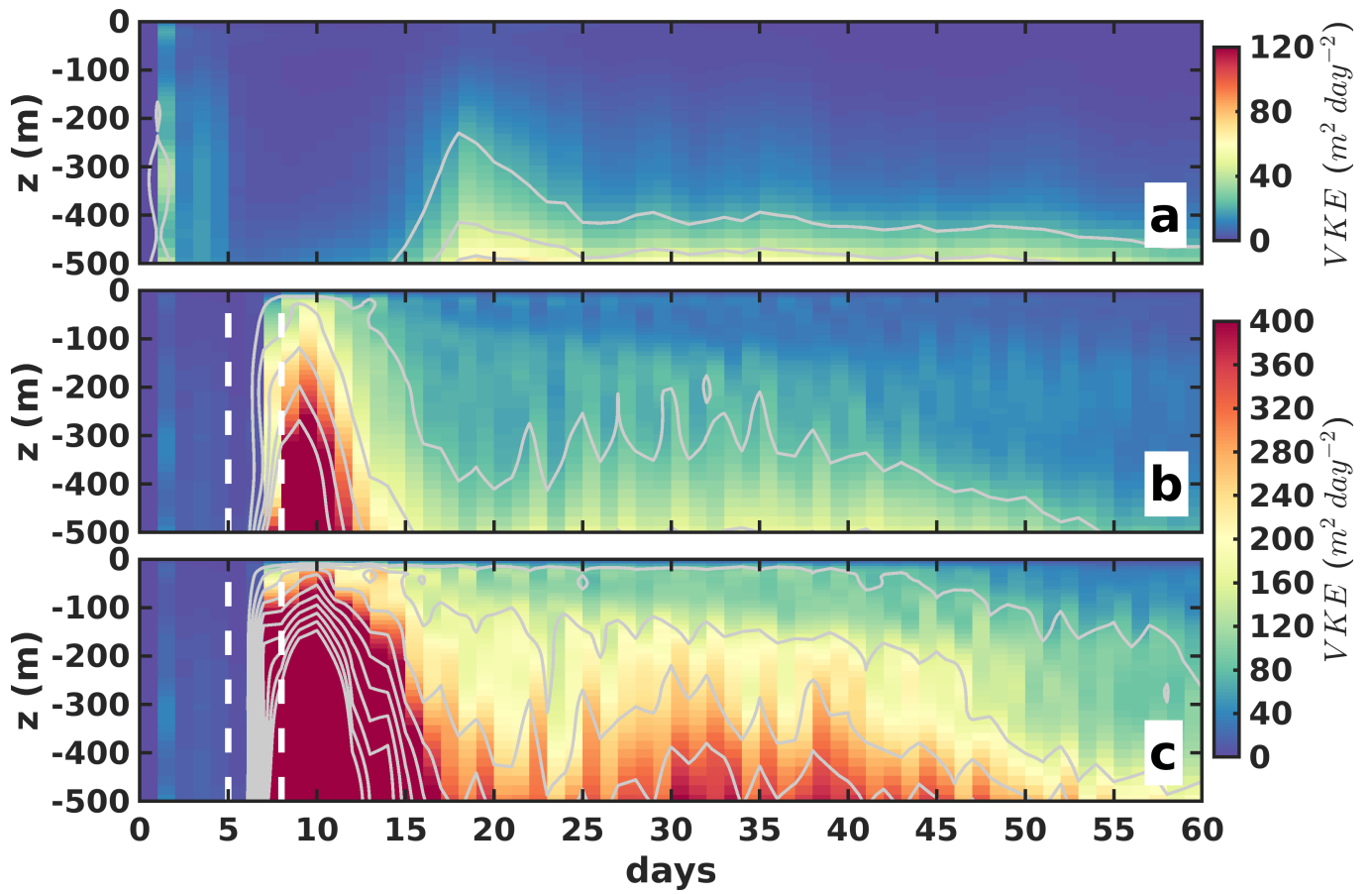


Fig. S6: (a), (b), (c) shows the Hövmöller of average of vertical kinetic energy (VKE) over the domain at per with the region of isospectra of the front (F), front with weak wave (F+WW), and strong wave cases (F+SW) for the upper 500 m. The white vertical dashed line shows the turning on (day 5) and off period (day 8) of the inertial wind.

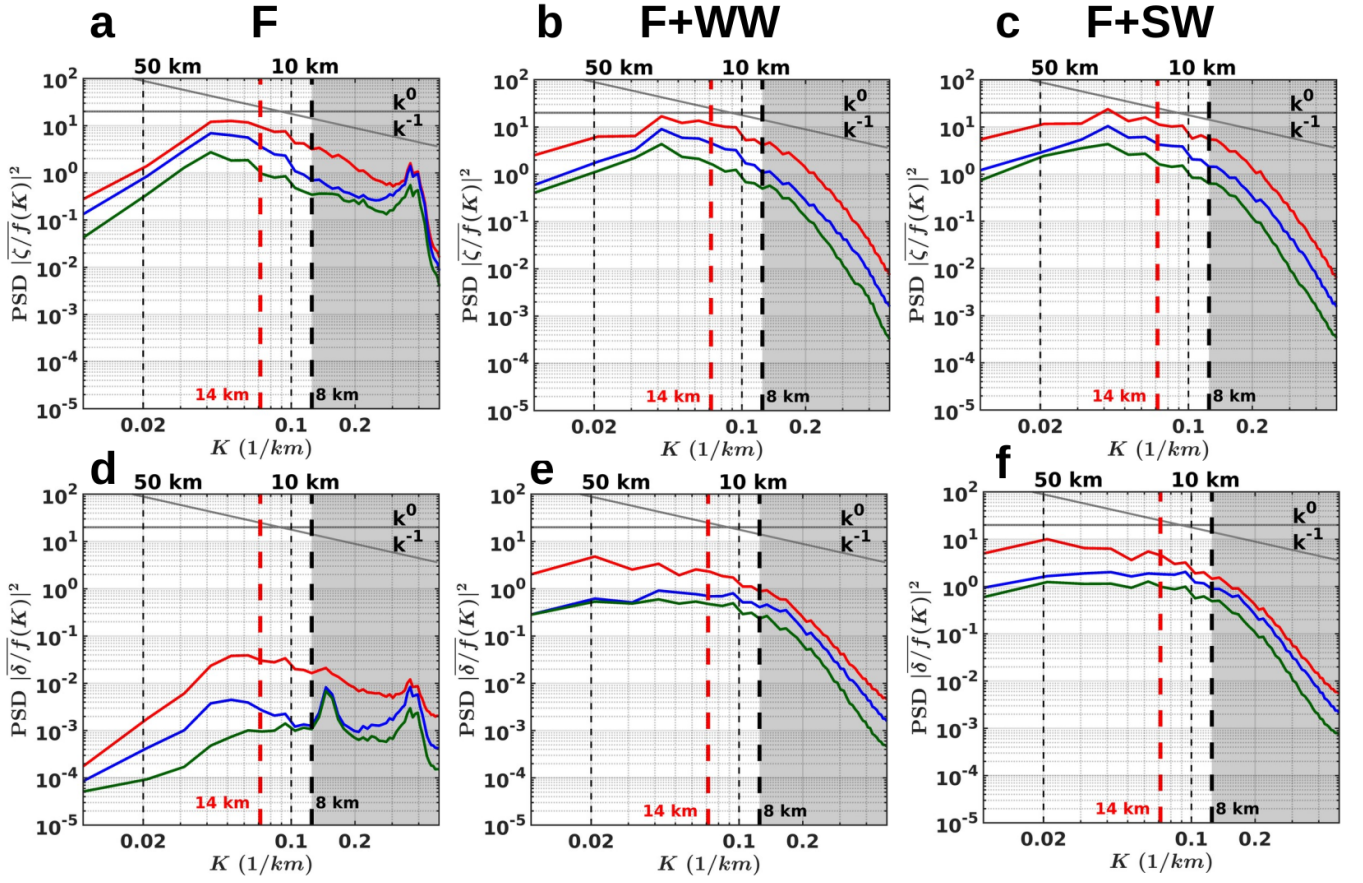


Fig. S7: (a–c) and (d–f) show the isotropic power spectral density of the normalized vorticity (ζ/f) and divergence (δ/f), respectively, as a function of horizontal wavenumber $K = \sqrt{k_x^2 + k_y^2}$, where k_x and k_y are the zonal and meridional wavenumbers (K in units of km^{-1}). Results are shown for the three cases—Front (F), Front with weak waves (F+WW), and Front with strong waves (F+SW)—over the period from day 8 to day 60 at depths of 3.5, 20, and 60 m. The gray lines in (a–e) indicate spectral slopes of 0 and -1 . The shaded region marks the unreliable part of the spectra ($K \leq 8$ km). The Rossby radius of deformation, $L_R = 14$ km, is indicated in red, as discussed in the text.

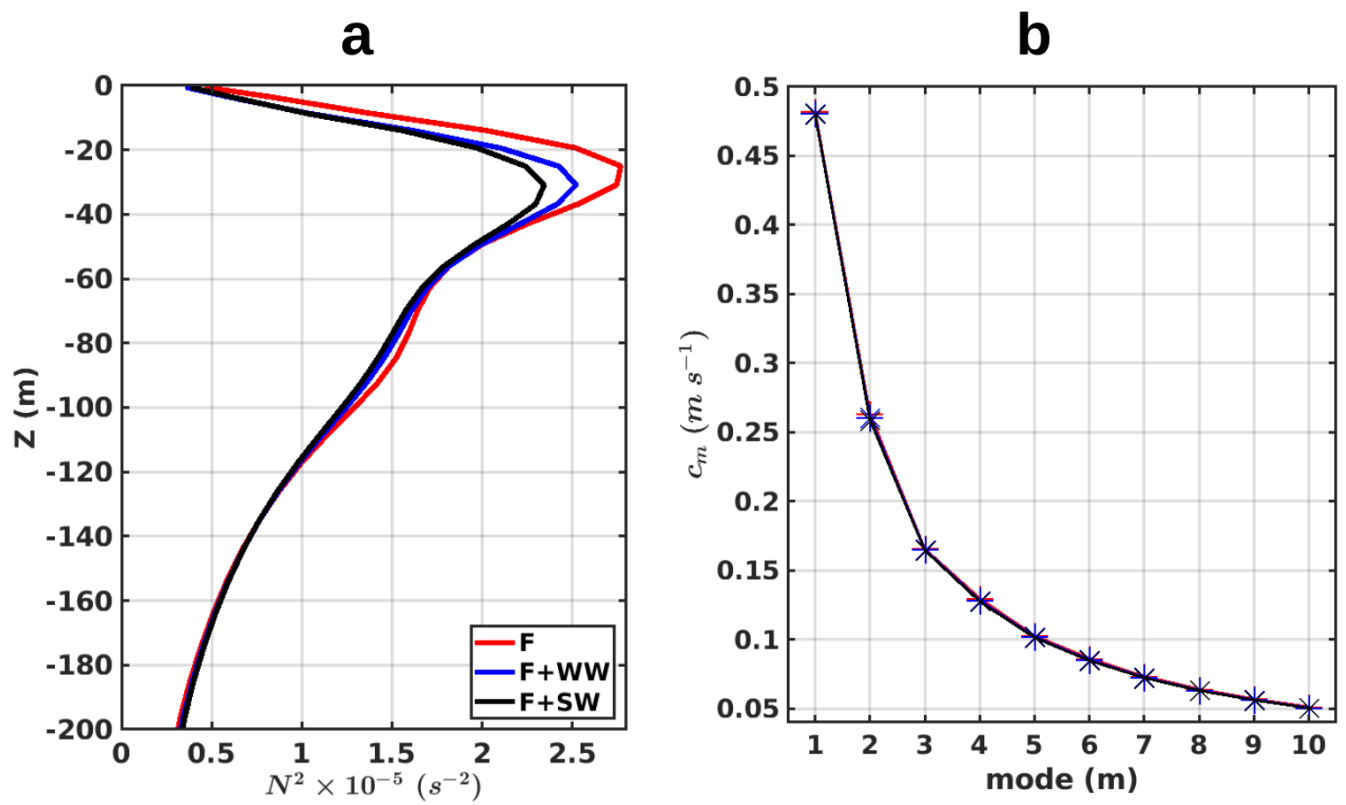


Fig. S8: (a) Time-mean squared buoyancy frequency (N^2) averaged over days 8–60. (b) Baroclinic phase speeds (c_m) for the first ten modes, compared among the F, F+WW, and F+SW experiments.

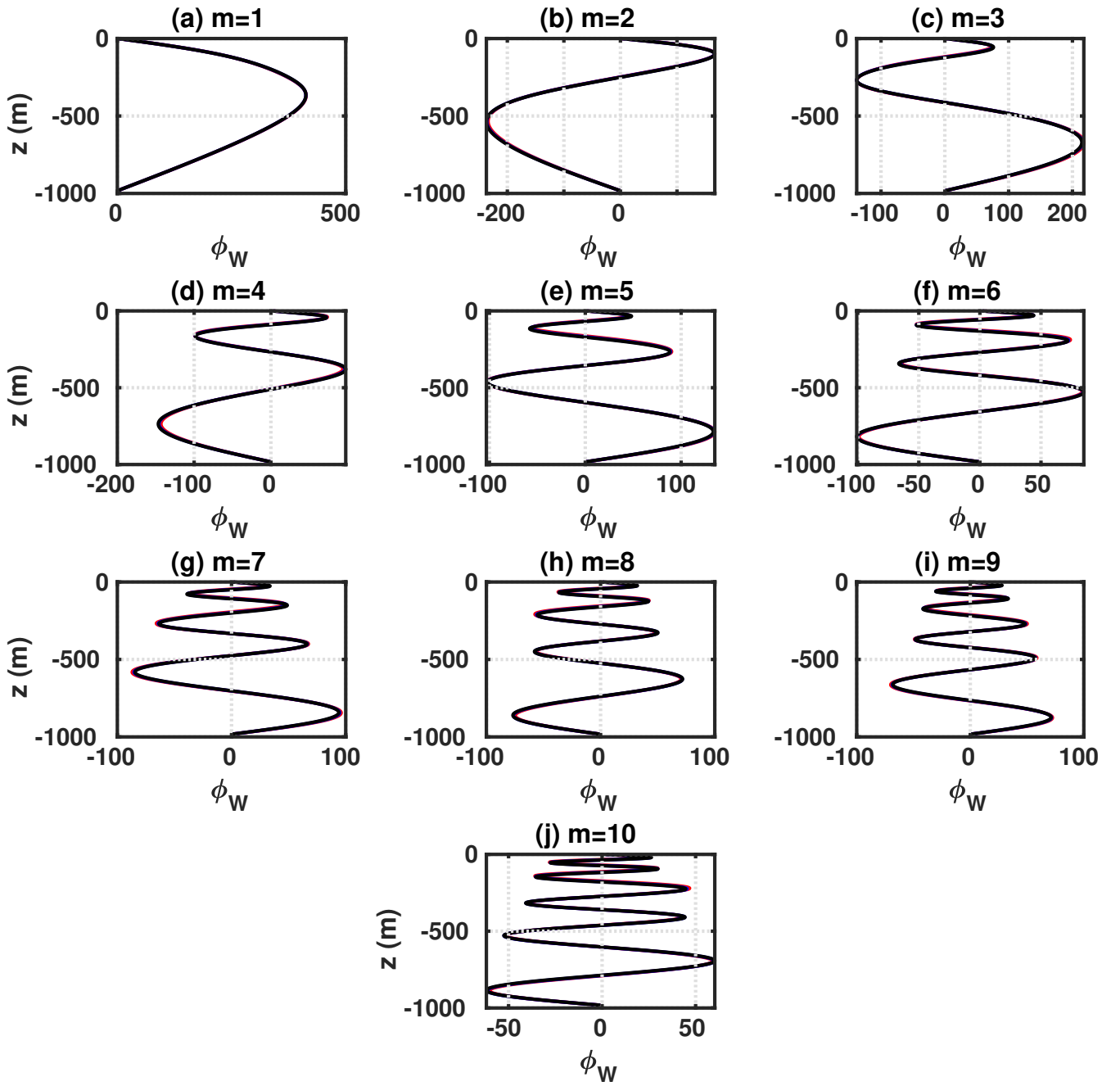


Fig. S9: Panels (a–j) display the eigenfunctions of the vertical velocity, ϕ_w , as a function of depth for modes $m = 1$ to $m = 10$. Results are shown for the three experiments: F (red), F+WW (blue), and F+SW (black).

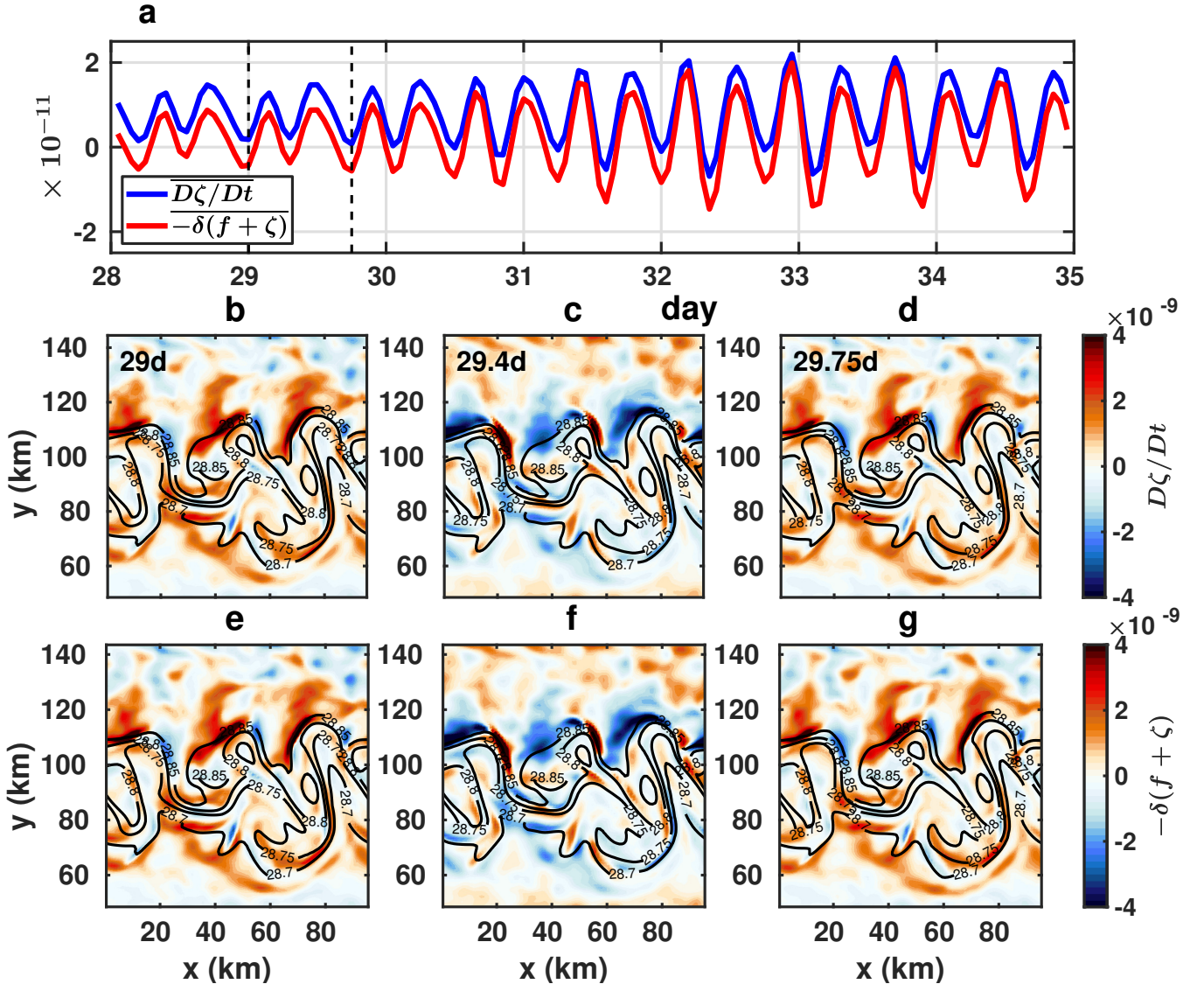


Fig. S10: (a) Domain-averaged $\overline{D\zeta/Dt}$ and $-\overline{\delta(f + \zeta)}$ as functions of time from day 28 to 35 at a depth of 3.5 m for the SW simulation. (b–d) and (e–g) show the spatial maps of $D\zeta/Dt$ and $-\delta(f + \zeta)$, respectively, over one inertial period at 29, 29.4, and 29.75 days overlaid with potential density contours. Dashed vertical black lines in panel (a) indicate the inertial period shown in the spatial maps.

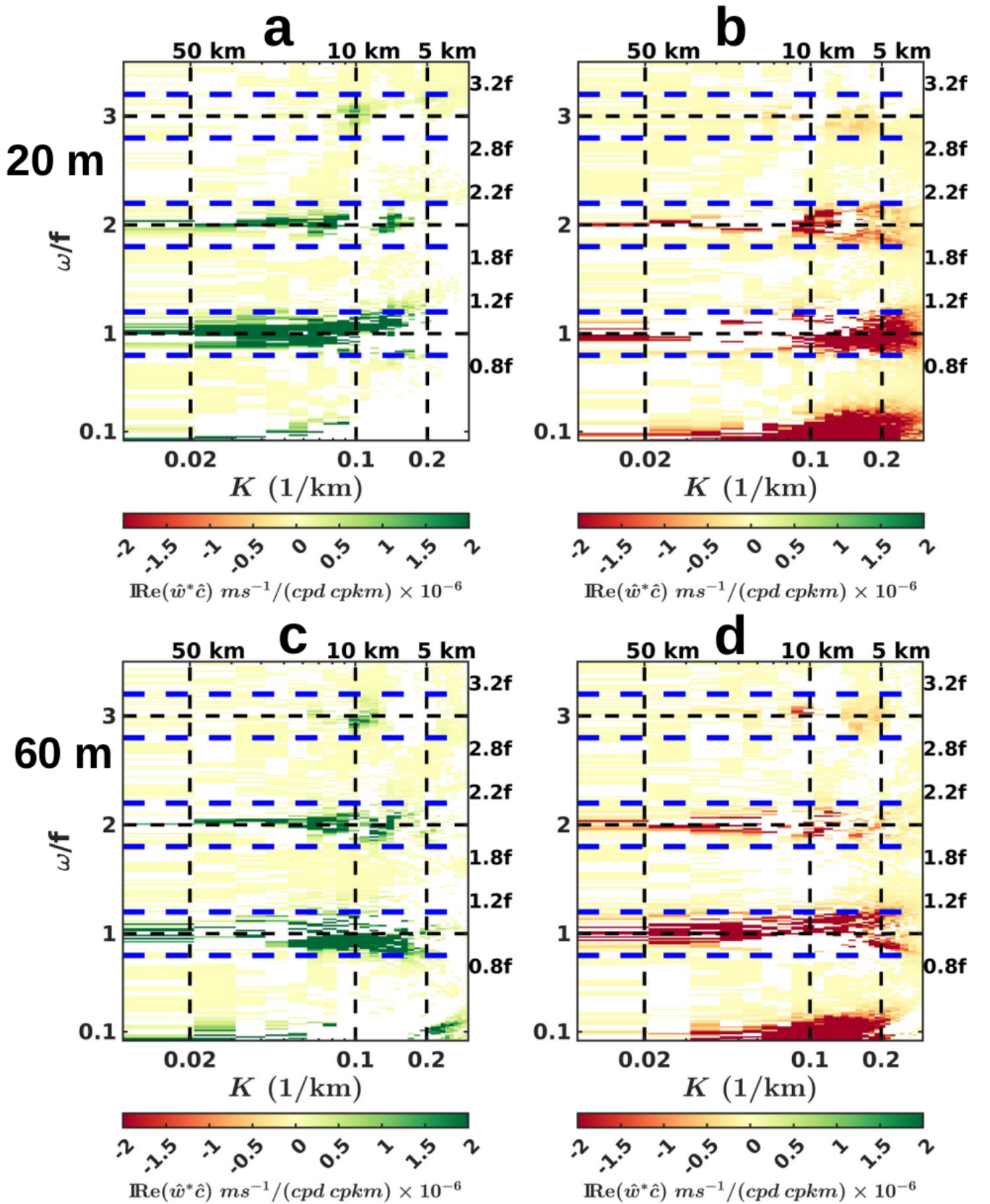


Fig. S11: Panels (a) and (c) show the positive, and panels (b) and (d) the negative components of the frequency–wavenumber isospectra of tracer covariances at 20 m and 60 m depth, respectively, for the F+SW experiment. The blue dashed lines indicate the inertial and superinertial frequency bands (f , $2f$, $3f$), each marked with an interval of $\pm 0.2f$ around the central frequency.

V. SUPPLEMENTARY TABLE

Barotropic/baroclinic speed ($m\ s^{-1}$)	wave	F	F+WW	F+SW
c_0		98.2124	98.2124	98.2124
c_1		0.4822	0.4811	0.4801
c_2		0.2635	0.2608	0.2581
c_3		0.1656	0.1651	0.1645
c_4		0.1298	0.1283	0.1274
c_5		0.1027	0.1019	0.1013
c_6		0.0863	0.0852	0.0846
c_7		0.0733	0.0727	0.0722
c_8		0.0641	0.0634	0.0630
c_9		0.0570	0.0564	0.0560
c_{10}		0.0512	0.0506	0.0503

Table. S1: Barotropic (c_0) and baroclinic wave speeds (c_m , $m = 1, 2, \dots, 10$) for the three experiments: F, F+WW, and F+SW.

VI. SUPPLEMENTARY MOVIES

Movie S1: (a) Free evolution of a density front (F). (b) Front with strong-wave (F+SW) forcing (inertial stress $|\tau| = 0.5 \text{ Pa}$). (c) No-front case with the initial stratification taken from the lighter side of the front and subjected to the same strong-wave (SW) forcing ($|\tau| = 0.5 \text{ Pa}$), with potential-density contours overlaid at a depth of -3.5 m . For the forced simulations, wind stress is applied from days 5–8 and ramped up and down using a Hanning window. The tracer is initialized on day 8 when the wind forcing is turned off. The quantity c' denotes the tracer anomaly relative to its distribution on day 8. The left color panel corresponds to the first row, and the right color panel corresponds to the second row.

Movie S2: (a) Relative vorticity with rotational velocity vectors. (b) Phase map of $\theta = \tan^{-1}(v_d/u_d)$, where u_d and v_d are the divergent velocity components, shown from day 28 to 35 for the F+SW case at -3.5 m depth. Contours of convergence/divergence ($|\delta/f|$) greater than 0.3 are overlaid, with convergence shown in dotted lines and divergence in dashed lines. (c) Vertical section along the thick black dashed line: rotational zonal velocity (u_{rot} , black contours) and potential density (green contours) with vertical velocity (shading). (d) Vertical tracer fluxes (shading) and the meridional divergent velocity component (v_{div} , black contours) with potential density (green contours), for the upper 100 m . The instances shown in this movie correspond to Figs. 8 and 9 in the main manuscript at 31.4 and 31.6 days, respectively.

SI text S1: Initialization of density front

The following tangent hyperbolic function has been used to create the front from the observation collected during the field campaign:

$$y_f(x) = \frac{L_y}{2} + A \sin\left(\frac{2\pi x}{L_x}\right); A = 1, \quad (8)$$

$$Thy(x, y) = 0.5\{1 + \tanh[2\pi B(y - y_f(x))]\}; B = 0.4, \quad (9)$$

$$\sigma_\theta = \sigma_{\theta_s}[1 - Thy(x, y)] + \sigma_{\theta_n}Thy(x, y). \quad (10)$$

where x, y are the coordinates with y_f as the center of the front, with L_x, L_y equals 96, 192 km representing the zonal and meridional extent of the domain given by Equation 8. The second term on the right side represents the wiggle added to the front to create the meander, with amplitude $A = 1$, along the zonal direction of one wavelength. The parameter B controls the meridional width of the stretch where the initial density values transition from south to north, with a value of 0.4 given by Equation 9. σ_{θ_s} , and σ_{θ_n} represent the southern and northern potential density anomalies, respectively, to create the front with the potential density anomaly (σ_θ) given by Equation 10.

SI text S2: Kinetic energy-wavenumber isotropic (radial) spectra

We adopt the methodology described in [15, 16, 59] and briefly illustrate it here. Let k_x, k_y , and $\hat{u}(k_x, k_y), \hat{v}(k_x, k_y)$ be the dimensional wavenumbers in the x and y directions, and the two-dimensional Fourier transforms of the velocity field. The horizontal wavenumber is defined by $K = (k_x^2 + k_y^2)^{1/2}$ with the integral of the spectral density of the two-dimensional kinetic energy (KE) $E(K)$ equal to the integral of the KE averaged over the domain given by Equation 11,

$$\left(\frac{\mathbf{u} \cdot \mathbf{u}}{2}\right) = \int_0^\infty E(K) dK \quad (11)$$

Let $\mathbf{c}(\theta) = (K \cos \theta, K \sin \theta)$ be represented in its parametric form; therefore, the $E(K)$ along the radial direction can be written as

$$E(K) = \frac{1}{2} \int_0^{2\pi} \{\hat{u}[\mathbf{c}(\theta)]\hat{u}^*[\mathbf{c}(\theta)]\} + \{\hat{v}[\mathbf{c}(\theta)]\hat{v}^*[\mathbf{c}(\theta)]\} K d\theta \quad (12)$$

The $E(K)$ from the horizontal velocities ($u_{r,s}, v_{r,s}$) is computed on the periodic mesh over the points of the grid N_x, N_y along x and y, given by

$$x_r = (r - 1)\Delta x, r = 1, 2, \dots, N_x, \quad (13)$$

$$y_s = (s - 1)\Delta y, s = 1, 2, \dots, N_y. \quad (14)$$

Then we use the Parseval theorem to convert from the discretized average KE to its two-dimensional discrete Fourier transform form in Equation 15,

$$\frac{1}{N_x N_y} \sum_{r=1}^{N_x} \sum_{s=1}^{N_y} u_{r,s}^2 + v_{r,s}^2 = \sum_{l=1}^{N_x} \sum_{m=1}^{N_y} \hat{u}_{l,m} \hat{u}_{l,m}^* + \hat{v}_{l,m} \hat{v}_{l,m}^* \quad (15)$$

Using the length of the domain as $L_x = N_x \Delta x$ and $L_y = N_y \Delta y$, we obtain $\Delta k_x = 2\pi/L_x$ and $\Delta k_y = 2\pi/L_y$; therefore, Equation 15 becomes

$$\frac{1}{L_x L_y} \sum_{r=1}^{N_x} \sum_{s=1}^{N_y} \frac{u_{r,s}^2 + v_{r,s}^2}{2} \Delta x \Delta y = \frac{L_x L_y}{8\pi^2} \sum_{l=1}^{N_x} \sum_{m=1}^{N_y} (\hat{u}_{l,m} \hat{u}_{l,m}^* + \hat{v}_{l,m} \hat{v}_{l,m}^*) \Delta k_x \Delta k_y. \quad (16)$$

We discretize the 2D wavenumber in multiples of the maximum one-dimensional wavenumber, $\Delta K = \max(\Delta k_x, \Delta k_y)$, such that

$$k_p = p \Delta K, \quad p = 1, 2, \dots, N_{max} \quad (17)$$

where, $N_{max} = \lceil \sqrt{2} \max(N_x/2, N_y/2) \rceil$. We then define $R(p)$ as the set of wavenumber indices (l, m) that satisfy the equation 18, and plot the spectrum $\tilde{E}(k_p)$ through the wavenumber $k_p = N \Delta K/2$.

$$k_p - \Delta K/2 \leq (k_{x_l}^2 + k_{y_m}^2)^{1/2} < k_p + \Delta K/2 \quad (18)$$

$$\tilde{E}(k_p) = \frac{L_x L_y \min(\Delta k_x, \Delta k_y)}{8\pi^2} \sum_{l,m \in R(p)} (\hat{u}_{l,m} \hat{u}_{l,m}^* + \hat{v}_{l,m} \hat{v}_{l,m}^*) \quad (19)$$

SI text S3: Frequency-wavenumber isotropic (radial) spectra

The frequency-horizontal wavenumber isotropic spectral density has been calculated from three three-dimensional discrete Fourier transforms following the methodology adopted from [60]. The three-dimensional Fourier transform of a variable η along the dimension corresponding to the indices q , g , and n given by

$$\hat{\eta}_{p,h,m}(k_p, l_h, \omega_m) = \sum_{q=0}^{Q-1} \sum_{g=0}^{G-1} \sum_{n=0}^{N-1} \eta_{q,g,n} e^{-2\pi i (\frac{pq}{Q} + \frac{hg}{G} + \frac{mn}{M})} \quad (20)$$

where, $\hat{\eta}$ is the Fourier transform corresponding to the indices p , h , and m as a function of k_p , l_h , and ω_m denoting the zonal, meridional wavenumber, and frequency. The length of the physical samples in the zonal, meridional, and temporal directions is given by Q , G , and N , respectively.

The spectral density $|\hat{\eta}(K, \omega)|^2$ associated with the r -th element of the isotropic wavenumber, k_r is given,

$$|\hat{\eta}_r(K_r, \omega)|^2 = \begin{cases} \frac{2}{QGN} \left[\sum_{p=1}^X \sum_{h=1}^Z |\hat{\eta}_{p,h}(k_p, l_h, \omega)|^2 \right], & \text{if } r = 1 \\ \frac{2}{QGN} \left[\sum_{p=1}^X \sum_{h=1}^Z |\hat{\eta}_{p,h}(k_p, l_h, \omega)|^2 \right] - \sum_{\gamma=1}^{r-1} |\hat{\eta}_\gamma(K_\gamma, \omega)|, & \text{if } r > 1 \end{cases} \quad (21)$$

where $k_\chi^2 + l_\zeta^2$, and r is an index that spans 1 to the length of K and $|\hat{\eta}(K, \omega)|^2$ is computed iteratively. The first term on the right-hand side of the equation is a sum over all values of $|\hat{\eta}(k, l, \omega)|$ for which p and h satisfy condition $k_\chi^2 + l_\zeta^2 < K_r^2$, and the second term on the right-hand side in the condition that $r > 1$ is a sum over all previously computed values of $\hat{\eta}_\gamma(K_r, \omega)$. The method conserves variance while transforming from anisotropic to isotropic spectral density.